



1 **Emerging mobile lidar technology to study boundary-layer** 2 **winds influenced by operating turbines**

3
4 Yelena Pichugina^{1,2}, Alan W. Brewer², Sunil Baidar^{1,2}, Robert Banta^{1,2}, Edward Strobach³,
5 Brandi McCarty^{1,2}, Brian Carroll^{1,2}, Nicola Bodini⁴, Stefano Letizia⁴, Richard Marchbanks^{1,2},
6 Michael Zucker^{1,2}, Maxwell Holloway^{1,2}, and Patrick Moriarty⁴

7
8 ¹CIRES, University of Colorado Boulder, Boulder, CO, USA

9 ²NOAA Chemical Sciences Laboratory, Boulder, CO, USA

10 ³AOSC University of Maryland, College Park, MD, USA

11 ⁴National Renewable Energy Laboratory, Golden, CO, USA

12
13 Correspondence to: Yelena L. Pichugina (Yelena.Pichugina@colorado.edu)

14

15

16 **Abstract.** The development of a microjoule-class pulsed Doppler lidar and deployment of this
17 compact system on mobile platforms such as aircraft, ships, or trucks has opened a new opportunity
18 to characterize the dynamics of complex mesoscale wind flows. The PickUp-based Mobile
19 Atmospheric Sounder (PUMAS) truck-based lidar system was recently used during the American
20 Wake Experiment (AWAKEN) to assess the general structure of boundary-layer wind and
21 turbulence around wind turbines in central Oklahoma.

22 Wind speed profiles averaged over PUMAS transects influenced by the operating turbines
23 (waked flow) show a 1–2 m s⁻¹ reduction compared to mean undisturbed (free flow) wind speed
24 profiles. Spatial variability of wind speed was observed in time-height cross sections at different
25 distances from turbines. The wind speeds were about 9–12 m s⁻¹ at 6 km distance compared to 5–7
26 m s⁻¹ at the transects near the turbines.

27 The PUMAS dataset from AWAKEN demonstrated the capability of the mobile Doppler
28 lidar system to document spatial variability of wind flows at different distances from wind turbines
29 and obtain quantitative estimates of wind speed reduction in the waked flow. The high-frequency,
30 simultaneous measurements of the horizontal and vertical winds provide a new approach for
31 characterizing dynamic processes critical for wind farm wake analyses.

32



33 1. Introduction

34 Stationary scanning Doppler lidars are a powerful remote sensing instrument that provide
35 high-quality measurements of wind and turbulence profiles from the surface up to several hundred
36 meters in the boundary layer. The Atmospheric Remote Sensing (ARS) group at the Chemical
37 Sciences Laboratory (CSL) of the National Oceanic and Atmospheric Administration (NOAA) uses
38 both commercial Doppler lidars and lidars developed within the group (Brewer and Hardesty,
39 1995). Lidar development at CSL goes back decades (Post and Cupp 1990_, Grund et al. 2002),
40 with continuous engineering updates and the design of new versions to meet research objectives.
41 Research studies on land using stationary scanning Doppler lidar have demonstrated the ability of
42 this instrument to reveal the structure and evolution of meteorological processes at a high vertical,
43 horizontal, and temporal resolution. Doppler lidar data are used to provide insight into boundary-
44 layer behavior during nocturnal stable and low-level jet (LLJ) conditions, among the most difficult
45 to characterize, understand, and model (Banta et al. 2003, 2006, Pichugina et al. 2010, 2023; Sun
46 et al. 2012). The lidar's three-dimensional (3D) scanning capability has been used to characterize
47 wind turbine wake properties and their downwind evolution, which is an important task for
48 optimizing wind farm layouts and power output. (Aitken et al. 2014; Banta et al. 2015, Bingöl et
49 al., 2010, Smalikho et al. 2013).

50 During the second Wind Forecast Improvement Project experiment, three scanning Doppler
51 lidars were deployed to the Columbia River Gorge to support the evaluation of the High Resolution
52 Rapid Refresh (HRRR) model, improve the prediction of winds in complex terrain (Olson et al.
53 2019; Banta et al. 2023, Pichugina et al, 2020, 2022), and to study wakes from the wind farm located
54 in the area (Wilczak et al. 2019). These studies used data from stationary Doppler lidars.

55 Motion-compensated lidar measurements from a mobile platform were obtained from a
56 NOAA research vessel in the Gulf of Maine. During these marine operations, the lidar was deployed
57 in a large seatainer with a GPS-based inertial navigation unit capable of determining platform
58 motion and orientation (Pichugina et al. 2012). A hemispheric scanner, mounted to the roof of the
59 seatainer, was controlled to compensate for pointing errors introduced by platform motion,
60 including those induced by ocean waves. The unique information obtained from this experiment
61 provided an opportunity for the first time to analyze the horizontal and vertical variability of marine
62 winds, offshore wind flow dynamics, and diurnal evolution of LLJ properties, and also to evaluate



63 model skill in an offshore setting, where high-quality wind measurements aloft are rare (Banta et
64 al. 2018; Djalalova et al. 2016; Pichugina et al. 2017a, 2017b).

65 Growing requirements for compact lidar configurations deployed on moving platform led
66 to the development of a new capability: a compact and robust microjoule-class pulsed Doppler lidar
67 system. Since 2018, the ARS/CSL group has focused on the development of such systems and
68 continuously updated design, measurement characteristics, and data acquisition techniques to
69 achieve the specific goals of each experiment.

70 The quantitative characteristics of wind and turbulence in the atmospheric layers occupied
71 by the wind turbine rotor blades (rotor layer) are crucial to wind energy, as is the information above
72 this layer to provide a meteorological context when considering profiles up to several hundreds of
73 meters above ground level (AGL). Furthermore, the region extending from the tops of the turbines
74 to the atmospheric boundary layer height plays a crucial role in the vertical entrainment of
75 momentum, which is an important driver of wind power capture (Meneveau, C. 2012;
76 Krishnamurthy et al. 2025).

77 Understanding the variability of winds across wind farms and under different conditions is
78 a critical factor in the planning and operation of wind projects. This goal can be achieved by
79 deploying a network of Doppler lidars over the wind farm or by taking measurements from a truck-
80 based mobile lidar. The accurate, motion-compensated measurements open an opportunity to
81 compare winds influenced by operational turbines (waked flow) with winds far from turbines (free
82 flow) along the driving path or to compare wind flows at different distances from turbine rows to
83 estimate the overall impact of the wind farm.

84 This paper aims to demonstrate the ability of truck-based Doppler lidar to provide high-
85 quality motion-compensated measurements in the boundary layer while driving around wind
86 turbines and present examples of analysis products obtained in August–September 2023 during the
87 multi-year American Wake Experiment (AWAKEN) campaign. Section 2 provides an overview of
88 ARS-developed mobile lidars, briefly describes technical parameters, motion-compensation, and
89 beam-stabilization systems, and discusses the lidar dataset. Section 3 presents the truck-based
90 mobile lidar, and discusses data obtained during an intensive operational period in Oklahoma.
91 Section 4 describes two case studies and provides analyses of the vertical, horizontal, and time-
92 evolving structures of wind flow in the presence of operating wind turbines for two selected days
93 characterized by differences in observed winds and boundary layer stability. Section 5 provides a



94 detailed analysis of the spatially and temporally varying structures of wind flow in the presence of
95 operating wind turbines for the two selected cases, showing wind speed and direction profiles at
96 various distances from turbines and comparing spatially distributed data from the mobile lidar with
97 data from nearby stationary Doppler lidars deployed in the research area. Section 6 contains
98 conclusions and recommendations.

99 **2. Development of the mobile micro-Doppler lidar system**

100 The compact micro-Doppler (MD) system deployment was achieved by a unique design of
101 a master oscillator power amplifier microjoule-class pulsed coherent Doppler lidar system in two
102 physically separated modules: the transceiver and the data acquisition system connected by an
103 umbilical cable (Schroeder et al. 2020). One module hosts the transceiver, which includes the
104 telescope, transmit/receive switch, and high-gain optical amplifier. The second module contains the
105 data acquisition system and several electro-optical components. This design, along with significant
106 decreases in the weight and the size of both modules, enables deployments of these systems on
107 small aircraft and pickup truck platforms that are otherwise inaccessible by commercial and
108 research instruments of similar design. The continuous updates and improvements of MD lidars
109 during the last several years led from version 1 (MD1) to version 3 (MD3). A detailed description
110 of versions MD1 and MD2, along with a short history of the development of stationary Doppler
111 scanning lidars in the NOAA/CSL ARS group, can be found in Schroeder et al. (2020).

112 Operation from a mobile platform faces many challenges, such as a constantly accelerating
113 reference frame and vibration while in motion. A significant obstacle to obtaining accurate wind
114 profiles from the high-precision lidar measurements using these techniques is compensating for the
115 pointing error and along-beam platform velocity due to platform motions. To address these issues,
116 the lidar is deployed with a *motion compensation* system that corrects the lidar velocity
117 measurement by estimating and removing the platform motion projected into the line-of-sight
118 velocity measurement in real time, and a *pointing stabilization* system that determines the platform
119 orientation and then actively stabilizes the orientation of the lidar beam in the world frame.

120 The development of the MD lidars and deployment of these compact systems on airborne,
121 shipborne, and truck-borne platforms (Figure 1) provided a new opportunity to study dynamic
122 processes in the atmospheric boundary layer in varied regions, from urban areas to remote locations



123 in complex terrain, and offshore. The flexible combination of temporal, vertical, and spatial
 124 coverage of the study area provides a significant advantage over stationary profiling observations.

125 The MD3 design was optimized for operation from pickup trucks and ships. The small
 126 modular footprint and weight of all subsystems allow their positioning in various compact spaces
 127 and enable easy stabilization. The MD3 lidar system features two laser transmitters and two
 128 channels to provide both continuous vertical-stare profiles of the vertical velocity w and,
 129 simultaneously, azimuth scans at 15° off zenith to give profiles of the horizontal wind speed and
 130 direction using the velocity-azimuth display (VAD) technique (Browning and Wexler 1968; Banta
 131 et al. 2002). The ability to do azimuthal scans at lower elevation angles, which can enhance
 132 accuracy in the horizontal VAD wind estimate (see Banta et al. 2023), is currently under
 133 development. The technical specifications of the MD3 lidar are given in Table 1.

134 Table 1. Typical specifications of the MD3 lidar

Pulse Length	30, 60, 90 m
Pulse repetition frequency	20,000 Hz
Beam rate	2–10 Hz
Pulse energy	50 μ J
Beam diameter	7.62 cm
Orientation	vertical
Maximum range	7 km
Electrical power	120 V, 30 A
Wavelength	1.553 μ m (invisible and eye safe)

135 Many portable configurations of remote sensing instruments currently used for various
 136 applications, including weather and atmospheric research, such as the Collaborative Lower
 137 Atmospheric Mobile Profiling System (<https://www.nssl.noaa.gov/tools/clamps>), are considered
 138 “mobile” systems. However, these systems must be delivered to the location of interest to provide
 139 a stationary measurement or be used in a “go-and-stop-for-measurements” pattern. In contrast, the
 140 mobile MD lidars developed at CSL/NOAA (Figure 1a–c) provide continuous measurements of w
 141 and horizontal winds while the platform is moving, which is a significant advantage compared to



142 the constraint of stationary Doppler lidars to obtain vertical and horizontal wind profiles at one
 143 location.

144 The truck-based measurements provide profiles of wind speed, wind direction, w , and aerosol
 145 backscatter intensity, showing the wind flow variability in time, with height, and along the moving
 146 path.



147
 148 Figure 1. NOAA/CSL Mobile Doppler Lidar Systems: (a) Ship-based; (b) Aircraft-based; (c) Truck-based.

149 The mobile lidar measurements have been used for various environmental studies. The multi-
 150 platform (aircraft and ground-based) setup was successfully used during recent wildfire and air-
 151 quality experiments, providing a unique opportunity to characterize atmospheric processes,
 152 including studies of fire plume transport dynamics, in better detail (Carroll et al. 2024; Strobach et
 153 al. 2023, 2024). The combination of spatial and temporal coverage of the aircraft-based mobile lidar
 154 measurements provides an advantage over traditional in situ or stationary profiling observations
 155 offshore and inland, for example, to study the air quality of large urban areas
 156 (<https://csl.noaa.gov/projects/aeromma/cupids/>). In the summer of 2024, the aircraft and truck-
 157 based modifications were involved in multi-institutional projects to estimate emissions of methane,
 158 greenhouse gases, and other significant air pollutants from oil and gas production facilities located
 159 in urban and agricultural areas of Colorado (<https://csl.noaa.gov/projects/airmaps/>). Table A1 in
 160 Appendix A shows a list of the CSL/NOAA field projects using mobile MD lidar on various
 161 platforms. The results obtained from these experiments use the high precision and excellent
 162 pointing accuracy of measurements from the ground-based, airborne, and shipborne deployments
 163 and demonstrate success in developing a fully capable mobile Doppler lidar for environmental
 164 studies.

165



2.1 Truck-based mobile lidar system

The latest version of the truck-based lidar system (Figure 2), the Pickup-based Mobile Atmospheric Sounder (PUMAS), was recently used to study the spatial structure of horizontal wind and turbulence near wind farms in Colorado and north-central Oklahoma.

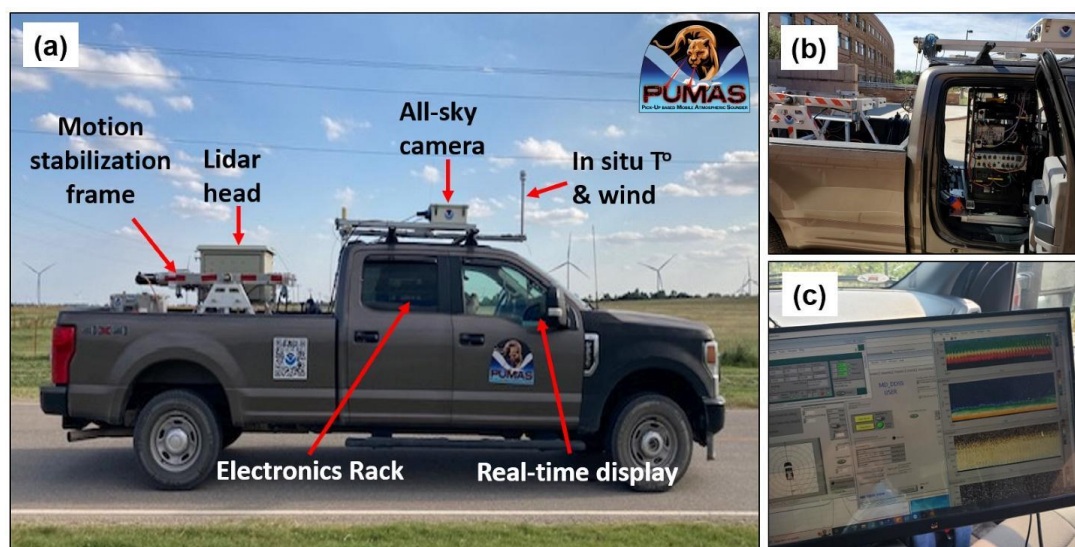


Figure 2. (a) Picture of PUMAS with indicated subsystems: Motion-stabilization frame, lidar head, all-sky camera, the sensor for in situ measurements of temperature (T°) and wind speed; (b) the electronics rack located in the back of a cabin; (c) real-time display located in the front of the cabin.

The PUMAS system (Figure 2a) included a motion-stabilization frame, the MD3 lidar head, an all-sky camera, and sensors for in situ temperature (T) and wind speed measurements. The electronics rack is located in the back of the cabin (Figure 2b), and the real-time display is in the front of the cabin (Figure 2c). PUMAS provided continuous motion-compensated measurements of wind flow and turbulence profiles driving on highways and dirt roads within wind farms. The two motion-stabilized lidar beams—vertically pointed and conically scanning with $\pm 15^\circ$ of zenith—provided simultaneous profiles of horizontal wind vectors, aerosol backscatter intensity, and w statistics from 60 m AGL to the top of the atmospheric boundary layer under normal atmospheric conditions and absence of precipitation. Data were obtained with a temporal resolution of 1–4 Hz and an along-beam resolution of 30 m. Wind speed profiles were obtained with an along-path resolution of 300–600 m, and w profiles every 10–30 m. Along-path resolution depends on the



186 driving speed and the road conditions but can be modified by changing accumulation time or scan
187 settings in the real-time display software.

188 During several pilot studies, PUMAS was tested around wind farms in Colorado (Appendix
189 B, Figure B1) to obtain information on system performance, measurement errors, and driving
190 strategies. The analysis of data from these test drives helped to set the science goals and a
191 measurement strategy for the participation of PUMAS in the AWAKEN campaign.

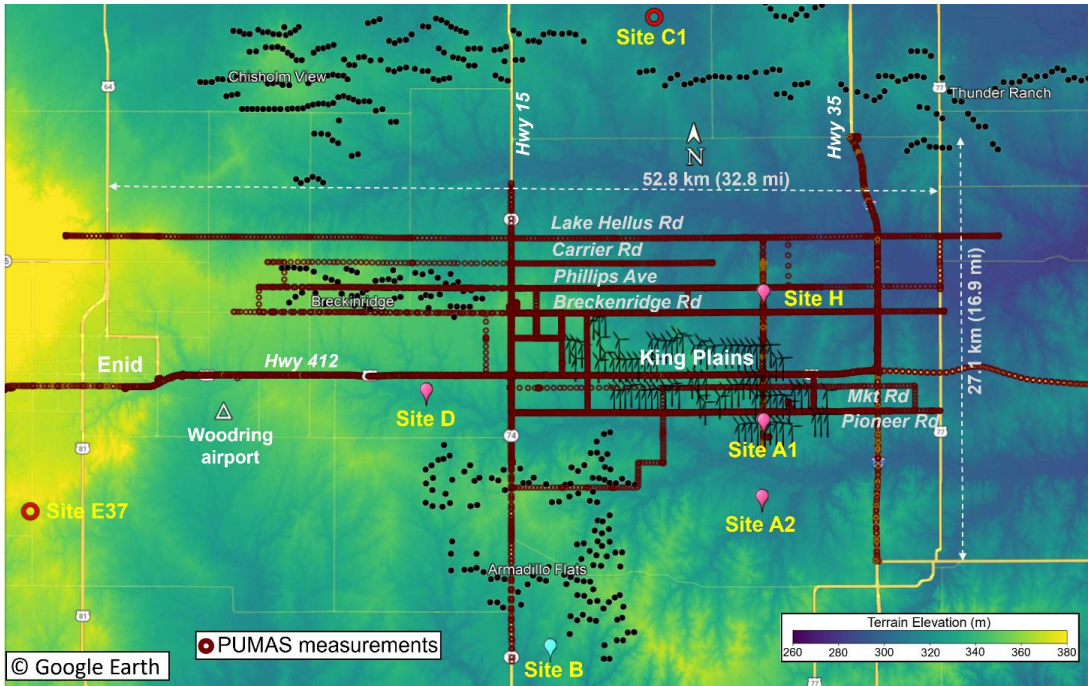
192 **3. American Wake Experiment**

193 The AWAKEN campaign is a U.S. Department of Energy (DOE) project led by the National
194 Renewable Energy Laboratory (NREL). It is a multi-institutional, long-term (2021–2025) study in
195 the U.S. Great Plains aiming to understand the interaction between wind farms and their
196 surrounding environment and improve the performance of wake models. Wind farms in the north-
197 central Oklahoma study area are located over relatively flat terrain (Figure 3a). More information
198 on the AWAKEN goals can be found here: <https://openei.org/wiki/AWAKEN>. Participating
199 organizations deployed various in situ and remote-sensing instruments to the study area, including
200 14 stationary scanning Doppler lidars and seven wind-profiling lidars. The full description,
201 measurement objectives, and locations of the AWAKEN instrumentation can be found in the
202 overview paper (Moriarty et al. 2024). The first benchmark study within the International Energy
203 Agency Wind Task 57 framework focused on wind plant wakes (Bodini et al. 2024). Detailed
204 information on the coordinated measurements from in situ and remote-sensing instruments,
205 including turbine nacelle-mounted lidars, is provided in AWAKEN-related papers (Bodini et al.
206 2024; Debnath et al. 2022, 2023; Krishnamurthy et al. 2021, 2025; Letizia et al. 2023; Moriarty et
207 al. 2024). The long-term measurements from scanning lidars (Newsom, R.K. and Krishnamurthy
208 R, 2020) at the Atmospheric Radiation Measurement (ARM) Southern Great Plains (SGP) and
209 AWAKEN sites provide additional information on wind and turbulence in the surrounding area
210 (Moriarty et al. 2024).

211 To support the AWAKEN science objectives, the CSL/ARS team operated PUMAS to
212 provide motion-compensated measurements of 3D wind flow and turbulence profiles from 15 Aug
213 to 12 Sep 2023. The measurements were mainly taken within and around the King Plains wind farm
214 (Figure 3), which comprised 88 General Electric wind turbines with a rated capacity of 2.82 MW,
215 a hub height of 89 m, and a rotor diameter of 127 m.



216



217

218 Figure 3. Wind farms in north-central Oklahoma are shown on the Terrain Elevation map (Debnath et al.
219 2022) by black dots. Turbine symbols show King Plains wind farm to underline the research focus on this
220 area. Red circles indicate the ARM SGP highly-instrumented Central Facility C1 and the extended facility
221 E37 (<https://www.arm.gov/capabilities/observatories/sgp>). Pink and cyan pins indicate AWAKEN lidar and
222 ASSIST sites used in this paper. The roads (transects), covered by PUMAS during AWAKEN, are shown
223 by dark red circles where each circle represents a profile measurement from 64 m up to several kilometers
224 AGL. The white triangle indicates the Woodring Regional Airport in Oklahoma, located about 8 km
225 southeast of the central business district of Enid, Oklahoma.

226 By considering the predominant wind direction estimated from various model forecasts at
227 the Enid Woodring Regional Airport in Oklahoma, a driving plan for each day was designed to
228 sample waked and free flows at various distances from the wind turbines (Figure 3). Transects were
229 repeated several times during 5–6 hours of measurements each day. At the beginning and end of
230 each transect, 5-minute measurements were made in a stationary position, and these data were used
231 to evaluate the system performance, as shown in Sect. 3.3.

232 In addition to PUMAS measurements, data from stationary Doppler lidars deployed at
233 various AWAKEN sites (Figure 3) were used for this paper. Data from the PNLL flux station were
234 used to estimate near-surface stability. Temperature and water vapor mixing ratios were estimated



through the TROPoe retrieval (Turner and Blumberg, 2018; Turner and Loehnert, 2014) based on observations from the NREL ASSIST-II spectroradiometer (Michaud-Belleau et al. 2025) measurements at Site B (Figure 3). The list of instruments used in the paper is given in Table 2.

Table 2. Coordinates of sites and types of instruments used in the paper.

Site	Latitude	Longitude		Instrument
PUMAS	varied	varied		NOAA/CSL motion compensated system with HALO XR lidar
H	36.4370	-97.4077	sh.lidar.z02.c1	AWAKEN scanning Doppler lidar HALO XR
A1	36.3623	-97.4078	sa1.lidar.z03.c1	AWAKEN scanning Doppler lidar HALO XR
A2	36.3182	-97.4090	sa2.lidar.z01.c1	AWAKEN scanning Doppler lidar HALO XR
			sb.met.z01.b0	PNNL flux station
D	36.3799	-97.6465	sd.lidar.z01	Fraunhofer IWES's WindCube v2.0
C1	36.6050	-97.4850	sgpdlprofwind4newsC1.c1	ARM scanning Doppler lidar HALO XR
E37	36.3110	-97.9280	sgpdlprofwind4newsE37.c1	ARM scanning Doppler lidar HALO XR
B	36.2316	-97.5587	sb.assist.z01.c0	Assist II-11

3.1 Meteorological conditions during PUMAS measurements in northern Oklahoma

According to the Oklahoma Climatological Survey (<https://www.ou.edu/ocs/oklahoma-climate>), the AWAKEN study area is in the North Central climate division. This northern section of the state is less influenced by the warm, moist air moving northward from the Gulf and experiences less cloudiness and precipitation compared to the southern and eastern portions of the state. Still, summers there are long and usually quite hot.

The surface wind statistics at the Enid Woodring Regional Airport, located 6.4 km southeast of downtown Enid, show predominant south-southeast wind directions in August and September 2023 and 5 m s⁻¹ mean winds with occasional gusts up to 10 m s⁻¹. The frequency of weak (1–4 m

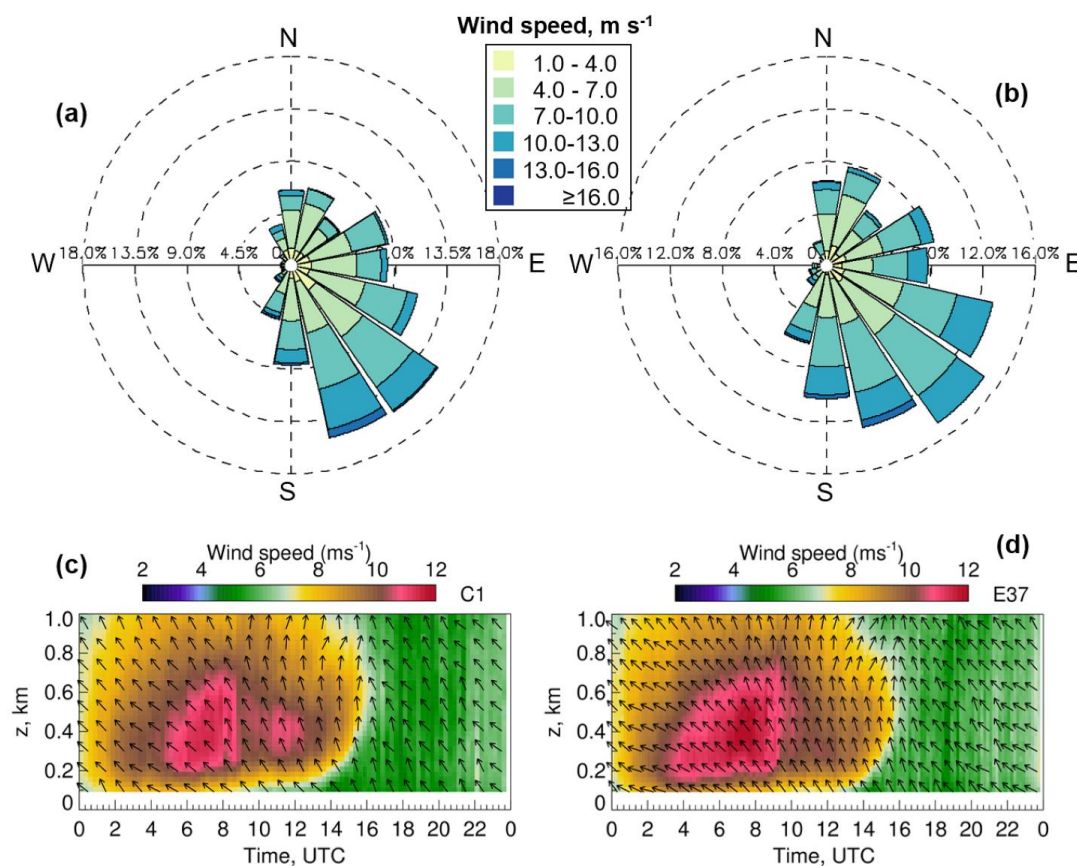


s⁻¹) winds is high for both months (71% in August and 63% in September), whereas stronger winds (4–11 m s⁻¹) were less common (17% in August and 25% in September). The August–September 2023 average temperature in Enid was 86–93 °F (30–34 °C) for the daytime and 68–73 °F (20–23 °C) for nighttime, with 20–22 sunny days each month and two rainy days on 13–14 September (www.windfinder.com/windstatistics/enid_woodring_regional_airport).

The ARM SGP atmospheric observatory with various in situ and remote-sensing instrument clusters located in north-central Oklahoma and south Kansas near the AWAKEN study area (Figure 3). The scanning Doppler HALO Photonics lidars provide long-term wind and turbulence measurements (Newsom R. K. and Krishnamurthy R. 2020) at the SGP central facility, C1, and four extended sites (E32, E37, E39, E41) and are used in many studies and experiments such as the Plains Elevated Convection at Night field campaign (Geerts et al. 2017) or the Land-Atmosphere Feedback Experiment (Wulfmeyer et al. 2018; Pichugina et al. 2023, 2024).

A 6-year analysis of (2013–2019) Doppler lidar data at C1 located north of the King Plains wind farm (Figure 3) confirms predominant southeast and south-southeast wind directions at 91 m AGL in August and September (Krishnamurthy et al. 2021). Another detailed study of winds from Doppler lidars at the five SGP sites revealed that the interannual (2016–2022) variability of monthly mean summer nighttime winds in the layer of 700 m AGL was more significant (4 m s⁻¹) compared to the wind variability (1–3 m s⁻¹) between sites, which are separated by 56–77 km, characterized by different vegetation types, and have elevations that vary between 279 and 379 m above sea level (ASL) (Pichugina et al. 2023). They also reported predominant south-southeast nighttime winds at all sites and frequent wind maxima at ~300 m.

Wind roses of 91 m winds from stationary Doppler lidar measurements on Aug. 15–Sept. 12, 2023, at two ARM SGP sites (C1 and E37) closest to the King Plains wind farm show wind directions from north to southwest with predominant southeasterly winds (Figure 4a, b). Time-height cross sections of winds averaged over 15 Aug–12 Sep 2023 (Figure 4c, d) were moderate (8–12 m s⁻¹) at night and weaker (4–6 m s⁻¹) during daytime. At both sites, wind directions below 300 m were primarily southeasterly, with some episodes of southerly winds at higher elevations. At C1 (Figure 5c), LLJ development is evident within 200–700 m AGL around ~0500–1200 UTC, whereas at the western E37 site, located 51 km to the southwest of C1 (Figure 3), the LLJ developed earlier in the 100–700 m layer.



278

279 Figure 4. Wind roses of 91 m winds from Doppler lidars at the ARM SGP sites (a) C1 and (b) E37 for all
 280 hours of measurements during 15 Aug-12 Sep 2023. (c, d) Time-height cross sections of period-mean wind
 281 speed (colors) and wind direction (arrows) from each Doppler lidar. Local Time=UTC-5.

282 3.2 Statistics of PUMAS measurements.

283 As mentioned, PUMAS participated in the AWAKEN experiment from 15 Aug to 12 Sep
 284 2023. Only 20 days of good measurements were available due to poor weather conditions (heavy
 285 rain) and technical issues such as flat tires or lidar-system-component issues. Four days were spent
 286 on a round trip between Boulder, Colorado, and Enid, Oklahoma. During each 982 km one-way
 287 commute, PUMAS provided continuous measurements of wind speed, wind direction, and w . The
 288 system performance was monitored and corrected as needed in real time, including motion-
 289 compensation parameters such as transceiver pitch, roll, and heading; platform velocity and
 290 coordinates; and estimates of the lidar beam azimuth and elevation in a world reference frame.

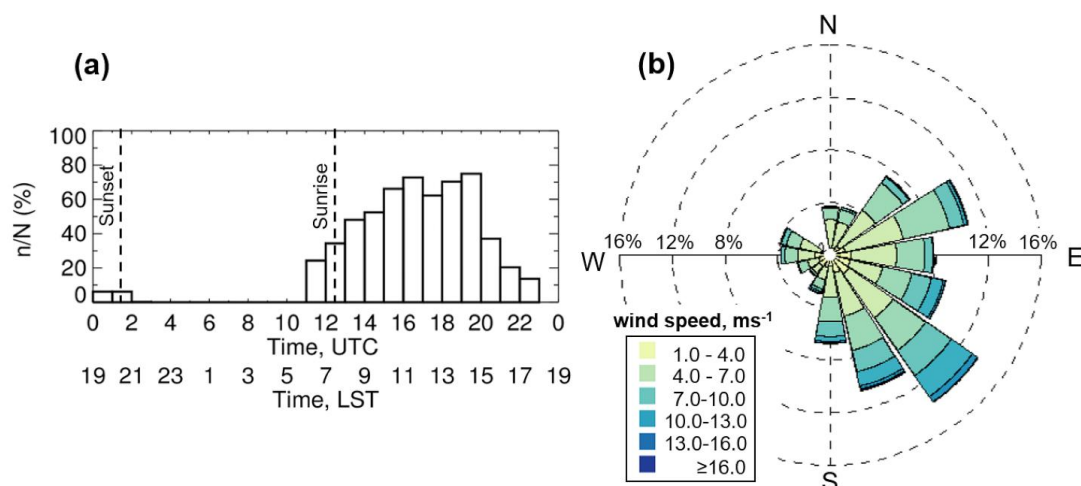


291 Overall, during the 20 driving days, PUMAS was on the road 81 hours, covering 3930 km
 292 (2443 mi) and providing 16,955 profiles of horizontal winds and w excluding data obtained during
 293 Denver–Oklahoma commutes.

294 The distribution of PUMAS operation hours (Figure 5a) shows that the most intense
 295 measurement period was in the late morning to midday (1500–2000 UTC). Nighttime
 296 measurements during stable conditions, when turbine wakes could be better observed due to the
 297 more substantial wind speeds and lower turbulence, were limited by the country road conditions
 298 and pure visibility of the upcoming crossroads traffic. It was expected that some events, such as the
 299 nocturnal LLJ, a frequent Great Plains phenomenon (Banta et al. 2002), would not be captured in
 300 the late mornings. However, the dissipation times of the LLJ often depend on synoptic conditions,
 301 and in some cases, LLJ can be observed after sunrise hours (Carroll et al. 2019; Squitieri B. J. and
 302 W. A. Gallus 2016; Pichugina et al. 2023).

303 The wind rose of the 64–160 m layer wind speeds (Figure 5b) shows the dominance of
 304 southeasterly winds during PUMAS measurements. Strong ($>15 \text{ m s}^{-1}$) winds were observed in
 305 13% of the southerly cases, followed by 10% in southeasterly and 7% in southwesterly directions.
 306 Based on the $d\theta/dz$ data from the ASSIST at Site B, the majority of PUMAS measurements were
 307 taken under unstable conditions (88.3%) as estimated from the ASSIST measurements at Site B.
 308 Stable conditions were observed in 7.8% of cases, and near-neutral conditions were observed in
 309 3.9% of cases.

310



311

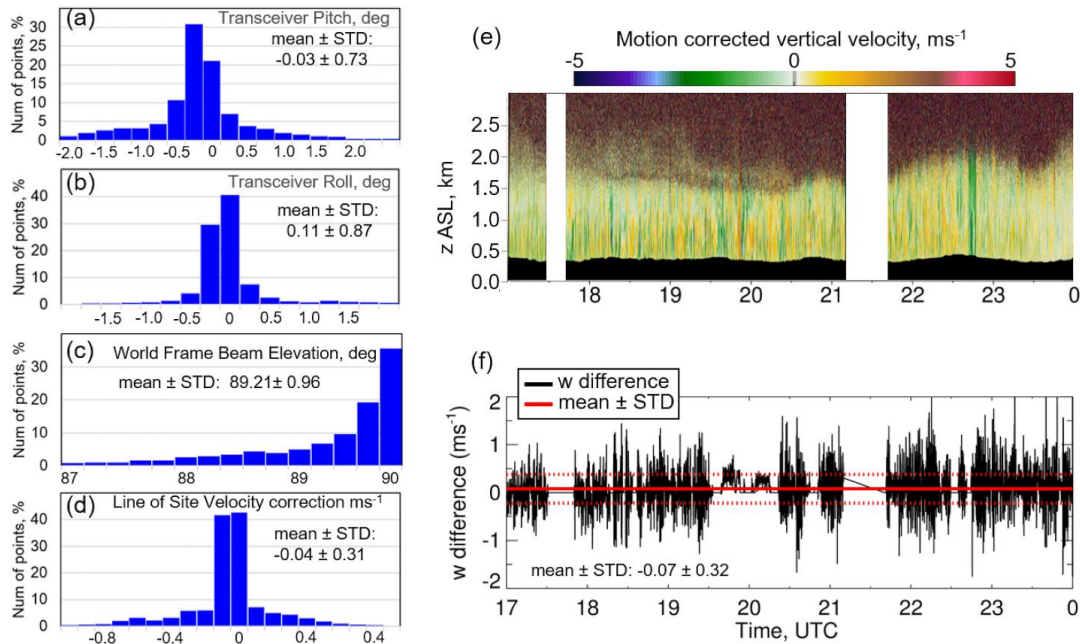
312 Figure 5. (a) Diurnal distribution of the PUMAS hours of operation during AWAKEN; (b) Wind rose of
 313 turbine level (64–160 m) winds from the PUMAS measurements.

314 3.3 Platform stabilization and motion correction

315 Active stabilization and pointing correction, implemented in the mobile lidar system,
 316 compensates for truck motions such as pitch and roll (Figure 6a, b) removing the effect of bumps
 317 on w while PUMAS is moving. In other words, the stabilization and motion-corrected system allow
 318 measurements of the w to be obtained without mixing in the projection of the horizontal wind speeds
 319 and their variation. Correction of the pitch and roll motions keeps the lidar beam elevation angle in
 320 a world frame at 89.21° on average with a standard deviation of ± 0.96 (Figure 6c) to obtain
 321 corrected line-of-sight velocity with an accuracy of $-0.04 \pm 0.31 \text{ m s}^{-1}$. An example of the motion-
 322 corrected vertical velocity from PUMAS measurements on 7 Sep (Figure 6e) shows significant
 323 turbulence in the first 1 km ASL and illustrates the 287–415 m variability of the terrain covered by
 324 PUMAS on this day. The mean difference between measured and motion-corrected w at 105 m
 325 (Figure 6f) is $0.08 \pm 0.32 \text{ m s}^{-1}$.

326

327



328

329 Figure 6. (a–d) Distributions (%) of the truck motion correction from PUMAS vertical velocity
 330 measurements on 15 Aug–12 Sep 2023, during AWAKEN. Mean \pm standard deviation (STD) is shown on
 331 the panel for each parameter. (e) A sample of motion-corrected vertical velocity measurements from 17:00
 332 to 24:07 UTC on 7 Sep 2023. Terrain elevation above sea level (ASL) covered by PUMAS on this day is
 333 shown in black. The white areas indicate missing data. (f) Time series of a (black) difference between
 334 measured and motion-corrected vertical velocity on 7 Sep 2023 at 105 m above ground level (AGL). Red
 335 solid line shows a period-mean difference. Dotted red lines show STD from the mean.

336 As mentioned, PUMAS provided 5–7 min of measurements in a stationary position at the
 337 beginning and the end of each transect. Measurements collected by PUMAS in a stationary position
 338 or while driving within a 2 km radius of a DOE stationary lidar at Site A1 or H are used to estimate
 339 the accuracy of PUMAS’s horizontal wind speed and direction by comparing the PUMAS and DOE
 340 lidar measurements as shown in Figure 7 and summarized in Table 3. The different number of wind
 341 speed and direction points (count) for each case is because the 3-sigma outlier rejection (see
 342 Pichugina et al. 2020) to the 1:1 fit was applied for speed and direction separately, leading to a
 343 different number of outlier points removed for speed and for direction. High correlation coefficients
 344 were obtained for wind speed (0.83–0.96) and wind direction (0.93–0.99) from PUMAS
 345 measurements in a stationary position and while moving except two cases when correlation
 346 coefficients were 0.65 between wind speed from the stationary PUMAS and Doppler lidar at Site
 347 A1, and 0.62 between wind direction from the moving PUMAS and Doppler lidar at Site H. The



larger offset in wind direction histograms was observed between PUMAS and Doppler lidar at Site
 H. Detailed analysis of these results is beyond the scope of this paper.

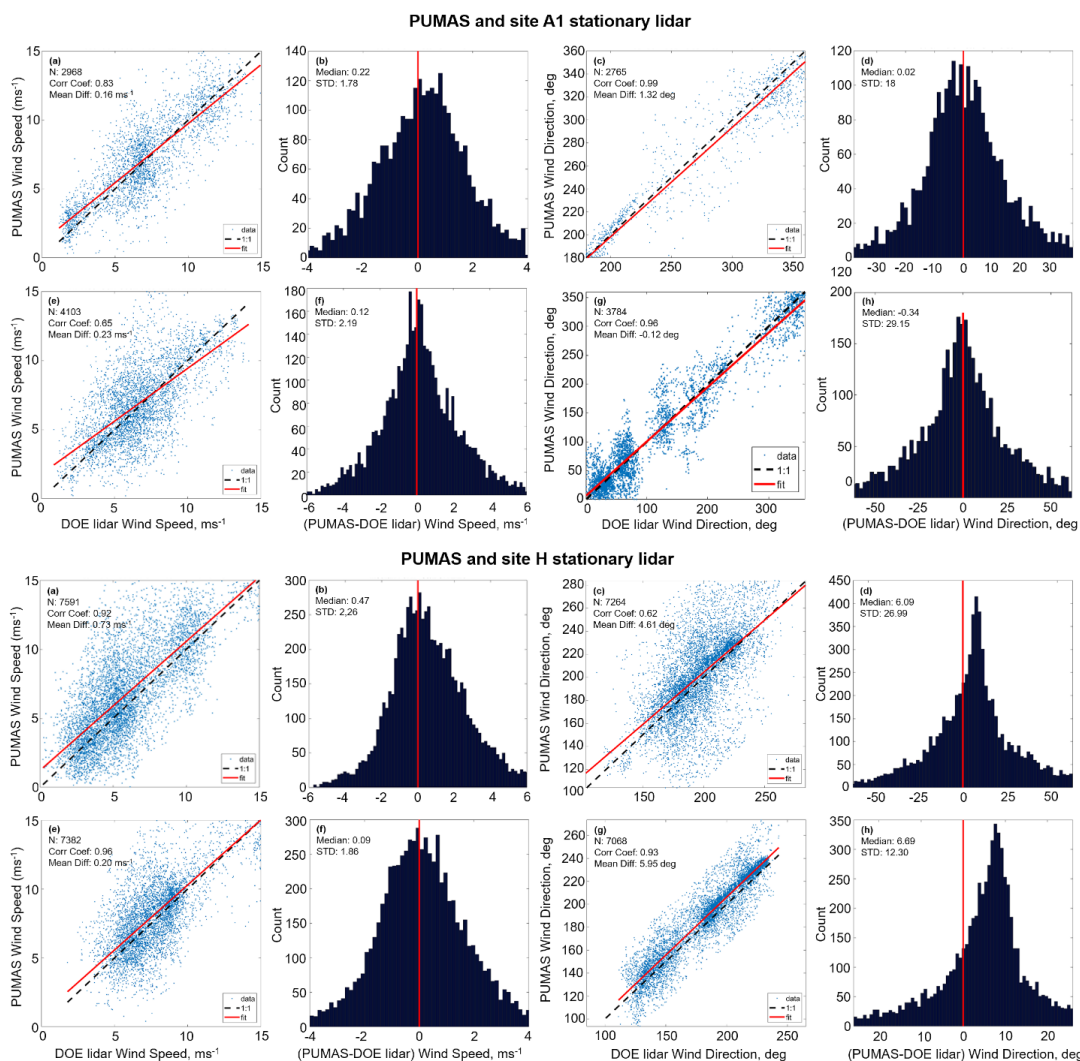


Figure 7. Comparison of horizontal wind and direction between PUMAS and DOE stationary Doppler lidar at Sites A1 and H: (a–d) from PUMAS measurements in stationary position collected within 2 km radius from DOE stationary Doppler lidar; (e–h) from moving PUMAS measurements collected within 2 km radius from DOE stationary Doppler lidar.



Table 3. Statistics from the comparison of wind speed and direction measurements from PUMAS and stationary Doppler lidars.

PUMAS vs. Stationary Doppler Lidar at Site A1						
PUMAS measurements	Data	Scatter plots statistics			Histogram statistics	
		Count	Cor Coef	STD	Medium	STD
Stationary	Wind speed	2968	0.83	0.16	0.22	1.78
	Wind direction	2765	0.99	1.32	0.02	18.0
While moving	Wind speed	4103	0.65	0.23	0.12	2.19
	Wind direction	3784	0.96	-0.12	-0.34	29.15
PUMAS vs. Stationary Doppler Lidar at Site H						
Stationary	Wind speed	7591	0.92	0.73	0.47	2.26
	Wind direction	7264	0.62	4.61	6.09	26.99
While moving	Wind speed	7382	0.96	0.20	0.09	1.86
	Wind direction	7068	0.93	5.95	6.69	12.30

Overall, Figures 6 and 7 and Table 3 clearly illustrate success in developing a fully capable mobile Doppler lidar that compensated for the truck's motions to provide accurate wind measurements. The uncertainty of the horizontal wind speed and direction estimated by the VAD technique (Banta et al. 2013) from PUMAS line-of-sight velocity measurements during AWAKEN was found to be very small with mean and standard deviations of $0.014 \pm 0.008 \text{ m s}^{-1}$ for wind speed and $0.12^\circ \pm 0.18^\circ$ for wind direction. The accuracy of motion-compensated measurements from mobile lidars was tested against stationary Doppler lidar measurements during several field campaigns. Examples of active stabilization and the accuracy of diurnal measurements from ship-based lidar during the offshore VOCALS campaign (Table A1) are provided in the Supplemental Material (S1a, b). Examples (S2a, b) illustrate a high correlation for wind speed (0.89, 0.90) and direction (0.93, 0.99) obtained from two experiments while PUMAS was driving within a 2.5 km radius from the stationary lidar (S2c) and when PUMAS provided measurements in a stationary position for several months (S2d).



374 **4. Selected case studies: 5 and 7 September.**

375 Two days, 5 and 7 Sep, were selected to illustrate the PUMAS measurements and analysis
 376 techniques. The data on these days were obtained during morning transition (5 Sep) and day-
 377 evening transition (7 Sep) periods, characterized by some difference in wind conditions and BL
 378 stability. Figure 8 shows wind speed (Figure 8a, c) and direction (Figure 8b, d) on these days from
 379 stationary Doppler lidars at SGP Site C1 (left) and SGP Site E37 (right).

380 **4.1 Wind speed and direction from stationary Doppler lidars**

381 On 5 Sep (Figure 8a, b), during a period of PUMAS operations in the early morning hours
 382 (1143–1645 UTC, 0543–1045 LST), both SGP lidars show strong ($15\text{--}25\text{ m s}^{-1}$) wind speeds and
 383 the development of the LLJ at 0200–1500 UTC (LST=UTC-5hours) with the LLJ maximum at 600
 384 m. Wind directions (Figure 8c, d) in the first 200–300 m AGL changed from southeasterly at
 385 nighttime, veering to southwesterly from late morning to afternoon and becoming northerly in the
 386 evening hours (after 1800 UTC). The wind speed ramp-down event observed at ~0900–1100 UTC
 387 below 400 m, is most likely another example of an atmospheric bore, as analyzed in this region by
 388 Pichugina et al. (2024). It corresponds to a transient shift to a more southwesterly wind direction.
 389 Such significant increases or decreases in wind speed lasting for a half-hour or more are difficult to
 390 forecast but may significantly affect turbine operations.

391 On 7 Sep (Figure 8e–h), both SGP lidars showed weak ($<4\text{ m s}^{-1}$) nighttime winds that
 392 increased to $8\text{--}12\text{ m s}^{-1}$ by 0900–1000 UTC (Figure 8c). The LLJ of $\geq 15\text{ m s}^{-1}$ developed at Site C1
 393 at 1400–1500 UTC below 400 m while stronger ($15\text{--}20\text{ m s}^{-1}$) LLJ developed at Site E37 around
 394 1300–1500 UTC below 300 m. Wind directions (Figure 8g, h) were primarily east-southeasterly
 395 ($100^\circ\text{--}150^\circ$) at both sites.

396

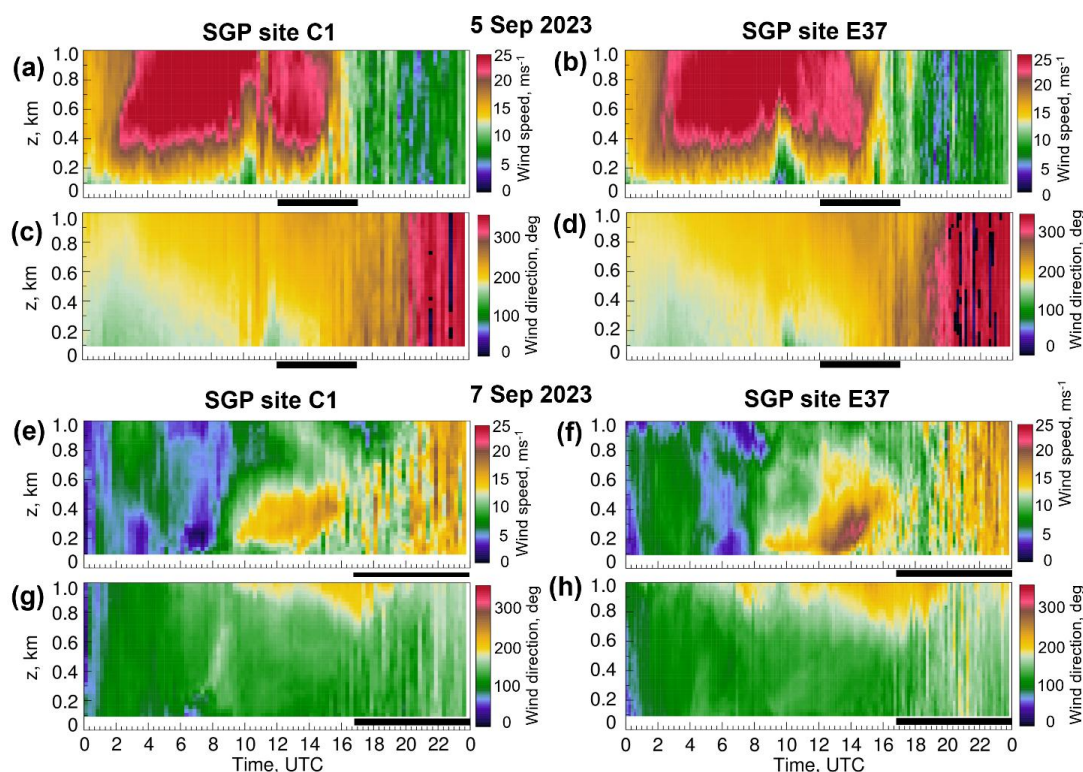


Figure 8. Time-height cross sections of wind speed and wind direction from stationary lidar measurements at the SGP Sites C1 (left) and E37 (right) measurements on (a–d) 5 Sep and (e–h) 7 Sep 2023. Black lines indicate periods of PUMAS measurements on these days. The temporal resolution of lidar data at C1 is 15 min and at E37 is 10 min. Lidar data at SGP sites can be found at the DOE ARM archive: <http://dx.doi.org/10.5439/1178582>.

Time series of wind speed and direction (Figure 9) at the six lowest heights from all stationary lidars depicted in Figure 4 also show similar trends in the evolution of wind flows, despite a significant distance between these instruments and locations at different terrain over the AWAKEN research area (Figure 4). In Figure 9, all lidars show highly variable wind speeds on 5 Sep, with an indication of a ramp event around 0900–1200 UTC and weaker, less variable winds on 7 Sep.

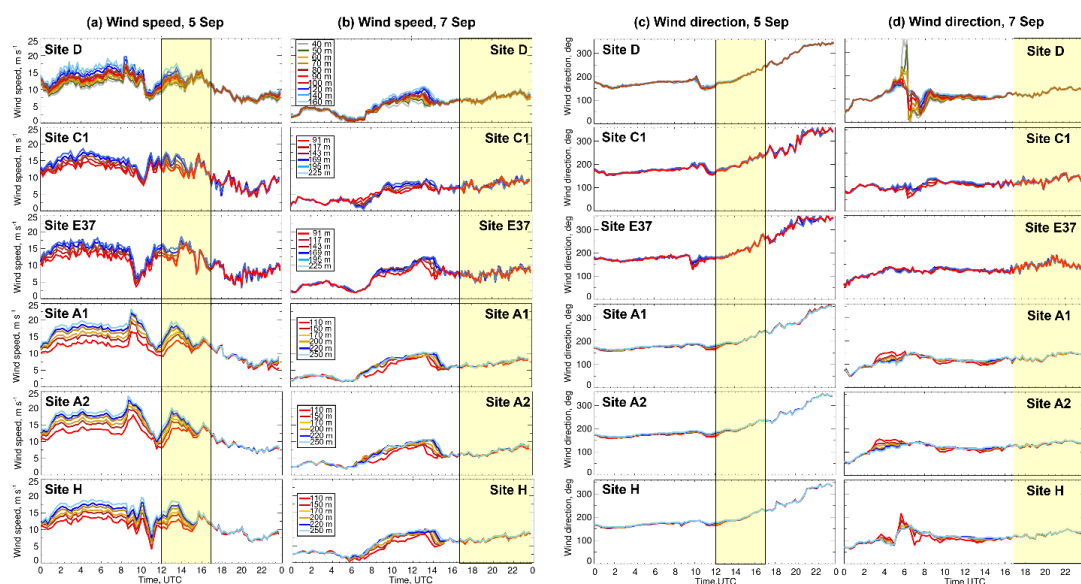


Figure 9. Time series of (a, b) wind speed and (c, d) wind direction from six stationary Doppler lidars at lowest heights on 5 Sep and 7 Sep. The location of lidar sites (Site D, Site C1, Site E37, Site A1, Site A2, and Site H) are shown in Figure 4. The heights of measurements are indicated in the legend for each lidar. Periods of PUMAS operations in a field on 5 Sep and 7 Sep are highlighted by the yellow color.

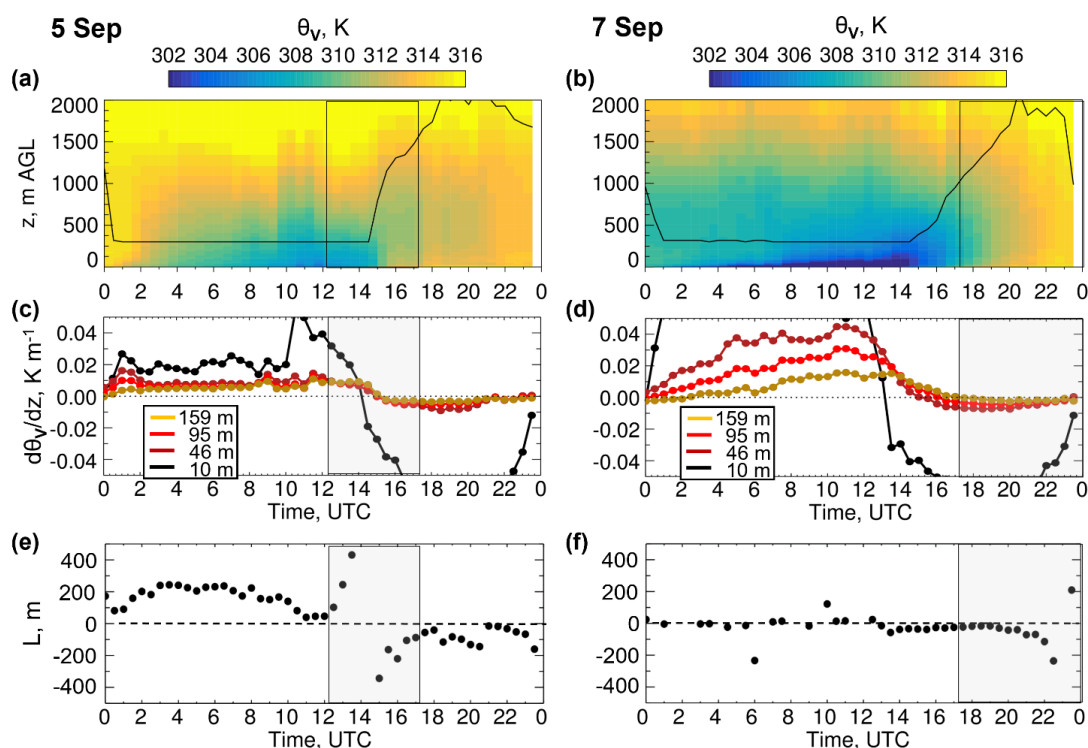
Interestingly, this pattern changed little between lidar measurements of inflow at Site A2 and waked flow at Site H during the period of PUMAS measurements highlighted by the yellow color (Figure 9). On 5 Sep, the mean wind speed at Site A2 was 0.8 m s^{-1} larger, and on 7 Sep, mean winds were 0.46 m s^{-1} weaker compared to Site H. The difference in wind direction between sites was 6.39° on 5 Sep and 7.83° on 7 Sep.

4.2. Stability on 5 and 7 September 2023

The virtual potential temperature (θ_v) computed from the TROPoe retrievals (Turner et al. 2014) of temperature and water vapor mixing ratio from thermodynamic profiler (ASSIST) data at Site B is shown (Figure 10a, b) for 5 Sep and 7 Sep. Stability estimates based on the virtual potential temperature gradient ($d\theta_v/dz$) show stable conditions at the beginning of PUMAS measurements on 5 Sep that changed to unstable by the end of the period (Figure 10c), whereas on 7 Sep, the unstable conditions were observed during all hours of PUMAS operations (Figure 10d). Sonic anemometer data from the PNNL flux station at Site A2 confirms the differences in stability between measurement hours on the two days (Figure 10e, f). Stability based on the Obukhov length



(L) threshold (Krishnamurthy et al. 2021) was stable at the beginning of PUMAS measurements on 5 Sep and changed to neutral in the middle and unstable at the end of this period (Figure 10e). On 7 Sep, very unstable conditions were observed at the beginning of the period changing to less unstable conditions by the end (Figure 10f).



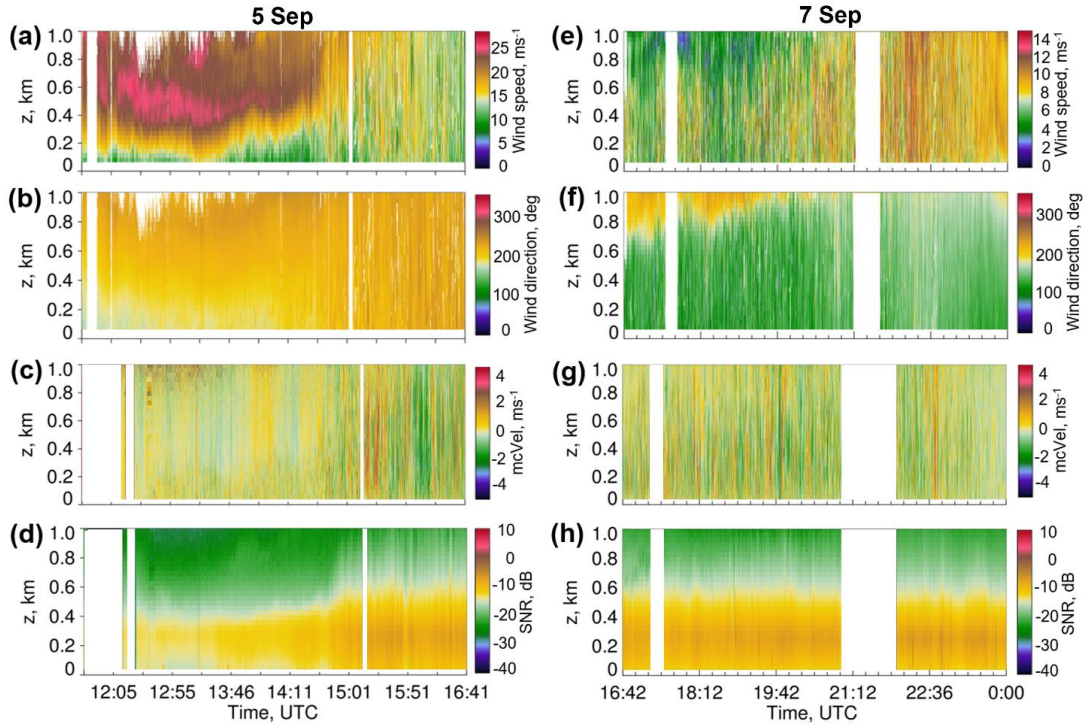
433

434 Figure 10. (a) Virtual potential temperature (θ_v) from ASSIST data at Site B on (a) 5 Sep and (b) 7 Sep.
 435 Black lines show planetary boundary layer height (m) derived from the retrieved fields. Virtual potential
 436 temperature gradient ($d\theta_v/dz$) on (c) 5 Sep and (d) 7 Sep at 10 m AGL and three heights within the limits
 437 of turbine blades. (e, f) Obukhov length from the PNNL flux station at Site A2 for these days. Gray shaded
 438 areas indicate periods of PUMAS measurement on each day.

439 5. PUMAS measurements on 5 and 7 September 2023

440 The PUMAS data, obtained with high temporal resolution and a significant spatial
 441 distribution over driving transects (see the following subsections), show a similar evolution of wind
 442 speed and direction to the stationary SGP lidars (Figure 8) for the period of PUMAS operations.

443



444

445 Figure 11. PUMAS-measured time-height cross sections of (a) wind speed, (b) direction, (c) motion-
 446 corrected vertical velocity, and (d) SNR (signal-to-noise ratio) intensity from simultaneous (Figure 11a, b,
 447 e, f) scanning and (Figure 11c, d, g, h) vertically-pointing data on 5 Sep (left column) and 7 Sep (right
 448 column). White areas indicate missing data.

449 On 5 Sep (Figure 11a–d), PUMAS measurements in the morning hours (1143–1645 UTC)
 450 show an LLJ mixing out after 1500 UTC. The data captured strong ($\geq 15 \text{ m s}^{-1}$) morning (~ 1200 –
 451 1500 UTC) wind speeds at higher elevations and the LLJ of $\sim 25 \text{ m s}^{-1}$ at 500–600 m (Figure 11a).
 452 The wind directions were predominantly south-southwesterly ($\sim 200^\circ$) with short periods of
 453 southerly winds below 200 m (Figure 11b). Stronger convective mixing was observed after 1500
 454 UTC (Figure 11c) as BL depth increased from 400 m to 600 m AGL (Figure 11d) and stability
 455 within rotor heights changed from stable to unstable (Figure 10c).

456 On 7 Sep (Figure 11e–h), PUMAS operated in the field for about 7 hours from late morning
 457 to the evening (1642–0007 UTC). Similar to 5 Sep, the agreement in trend (wind speeds increasing
 458 through the period) between data from stationary SGP lidars and PUMAS measurements was
 459 evident, although PUMAS sampled somewhat weaker winds. The daytime (1642–2100 UTC),
 460 southeasterly (120° – 140°) winds of 5 – 8 m s^{-1} increased by the evening to 10 – 12 m s^{-1} (Figure 11e),

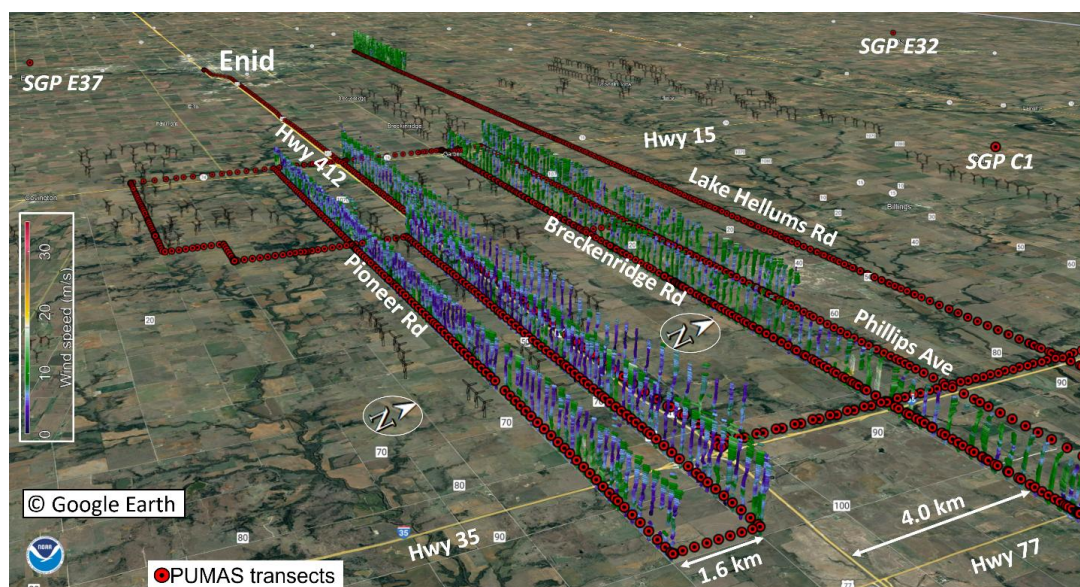


461 and veered to south-southeasterly (160° – 170°) below 600 m (Figure 11f). The steady mixing with
 462 the BL height to >600 m was observed during most of a period (Figure 11g, h) characterized by the
 463 unstable BL conditions (Figure 10d).

464 The next sections will provide a closer look at PUMAS measurements during selected
 465 days starting with 7 Sep, the longest period of measurements characterized by moderate (6 – 12 m
 466 s^{-1}) wind speed and unstable BL conditions, which were common for most days during PUMAS
 467 operations.

468 5.1 7 September case study, southeasterly winds

469 Throughout the previous sections, 5 Sep was discussed first, then 7 Sep. Here, we change
 470 the order and start with the case study on 7 Sep, as it was the longest period of PUMAS
 471 measurements, and these data were taken during the most frequent (Figure 5a) late-morning (1600 –
 472 2000 UTC) hours. Relatively calm wind speeds and southeasterly directions this day are more
 473 common for many other days in contrast to the 5 Sep case of strong, southwesterly winds. On 7 Se,
 474 PUMAS operated in the field for about 7 hours and 25 min (1642 – 0007 UTC), covering more than
 475 422 km. A 3D visualization of wind profiles (Figure 12) measured on 7 Sep along several transects,
 476 out of 34 total for the day, illustrates stronger (≥ 10 m s^{-1}) winds in green colors compared to weaker
 477 (≤ 5 m s^{-1}) winds shown by purple colors.





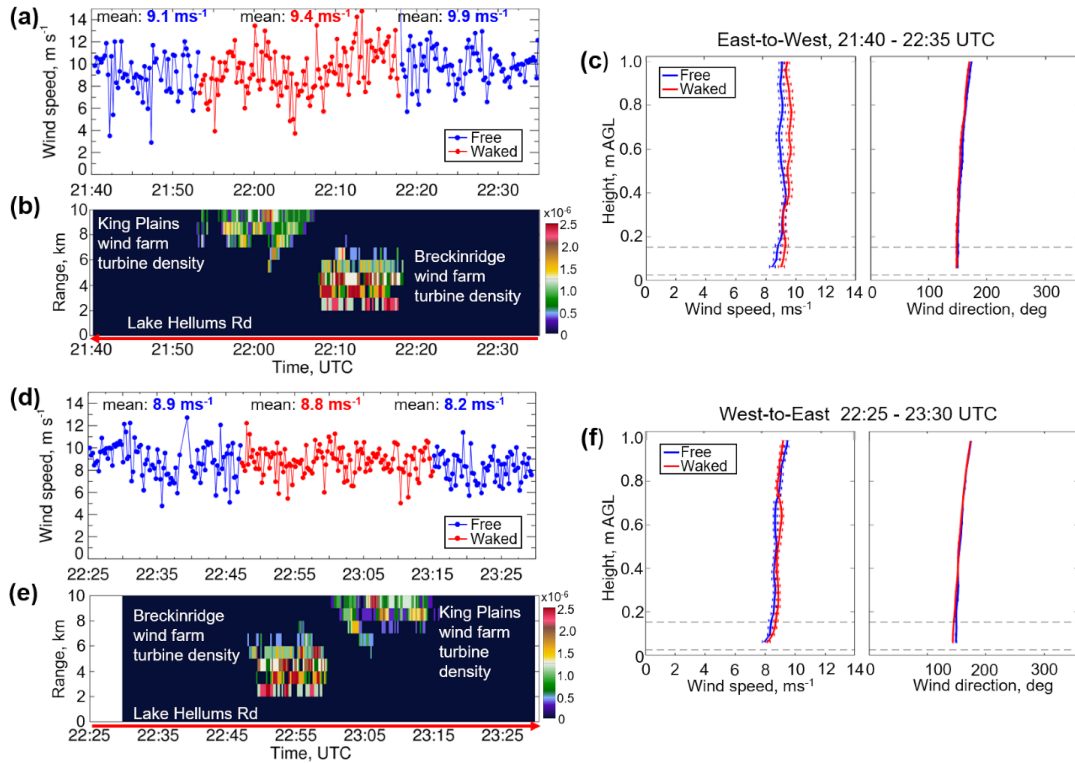
479

480 Figure 12. Samples of wind profiles along some transects on 5 Sep 2023, embedded on Google Earth, are
 481 rotated clockwise $\sim 45^\circ$ for a better view. Profiles are shown up to 1.5 km AGL, and wind speed is scaled
 482 from 0 to 30 m s^{-1} according to the color scale on the left side of this figure. The horizontal distance between
 483 profiles is about 300 m. White arrows indicate distances between illustrated transects along the named roads.
 484 Gray circles indicate the ARM SGP sites (C1, E37, and E32).

485 5.2 Technique to estimate free and waked flows

486 A technique to estimate wind speed for sections of a transect that are in the shadow of wind
 487 turbines (waked flow) or free from the turbine influence (free flow) is based on the density of
 488 upstream wind turbines that may impact wind measurements, computed within 10 km from the road
 489 (Figure 13b, e) including all Breckinridge wind farm turbines located within 2–4.7 km from this
 490 road (note a slight spelling difference in the road and wind-farm names). This example did not
 491 consider some of the King Plains and all Armadillo Flats turbines located more than 10 km from
 492 the road. The influence of turbines on wind-speed measurements (turbine shadow) was estimated
 493 within a 20° arc ($\pm 10^\circ$ turbine shadow) from each point of a PUMAS measurement of wind
 494 direction. Sections of a transect indicated by red in the wind time series (Figure 13a, d) are
 495 considered waked, whereas those considered as not influenced by wind turbines (free flow) are
 496 blue.

497 Figure 13 a, d shows time series of the rotor-layer (64–150 m) mean wind speed measured
 498 during the east-to-west (EW, 59.2 km) and west-to-east (WE, 55.4 km) transects on Lake Hellums
 499 Rd. (Figure 12). Mean rotor-layer winds in the free-flow sectors along the EW transect increased
 500 from 9.1 to 9.9 m s^{-1} , whereas on the return WE transect, the winds decreased from 8.9 to 8.2 m s^{-1} .
 501 The free-flow wind speeds were thus stronger for the western sector by 0.7–0.8 m s^{-1} , most likely
 502 due to terrain differences, and the winds slowed by $\sim 1 \text{ m s}^{-1}$ in the time between the two sampling
 503 legs. Significant spatial variation of the wind speed within both the waked flow and the free flow
 504 sectors reflects the significant natural atmospheric variability characteristic of this midday
 505 convective period and appears larger than the mean speed differences between waked and free flow
 506 regions.



507

508 Figure 13. Time series of wind speed averaged over the rotor-layer (64–159 m) height from PUMAS
 509 measurements on Lake Hellums Rd. during (a) east-west (49.3 min) and (b) west-east (54 min) transects.
 510 Blue indicates free wind flow that is not influenced by wind turbines, and red indicates waked wind flow.
 511 The density of Breckinridge and King Plains wind turbines is computed within 10 km from the PUMAS
 512 transects. (c, f) Mean wind speed and direction profiles at each transect for parts of (blue) free and (red)
 513 waked flows.

514 The mean profiles of free-flow and waked winds are shown in Figure 13c,f. Within the
 515 turbine layer mean waked speeds were slightly ($<1 \text{ m s}^{-1}$) larger than the mean free-wind values for
 516 the EW transect (Figure 13c), contrary to expectation, but comprehensible in light of the variable
 517 nature of the convective BL. Within 200–400 m, these profiles are the same, deviating again at
 518 higher levels. During the WE transect (Figure 13f) both free and waked profiles were very similar.
 519 Mean profiles of wind direction for waked and free winds are close for both EW and WE transects,
 520 turning from 140° within the rotor layer to 175° at 1 km AGL. The statistically insignificant
 521 difference between mean waked and free wind speed profiles in this example resulted from the
 522 temporal evolution of winds over 55 min drive one way.



523 The rotor-layer-mean waked flow from the Breckinridge wind farm was 8.8 m s^{-1} compared
524 to 10 m s^{-1} of waked flow downwind of the King Plains wind farm (Figure 13b). The difference in
525 waked flow between the Breckinridge (8.7 m s^{-1}) and King Plains (8.3 m s^{-1}) wind farms is much
526 smaller on the way back (Figure 13d). As stated previously, these differences are primarily due to
527 the temporal variability of wind speed and a slope of a terrain along Lake Hellums Rd., which
528 descends from 400 m on the west to 280 m on the east.

529 The developed technique allows waked and free flows from measurements at different
530 distances from turbines to be estimated as illustrated in Figure 14 for the following transects:
531 (Figure 14a) within King Plains wind farm on Hwy 412; (Figure 14b) on the Breckenridge Rd.
532 located 0.9 km of the wind farm; and (Figure 14c) on Lake Hellums Rd. located 5 km north of the
533 turbines (Figure 4). Profiles show free-stream winds at locations within the wind farm $1\text{--}1.5 \text{ m s}^{-1}$
534 stronger than waked winds there, as expected, and the difference decreases with distance from the
535 farm, until at 5 km (Figure 14c), the waked and free flow profiles are equal within the standard-
536 deviation error. Wind directions of waked and free flows at each transect (Figure 14a–c) remain
537 southeast below 500 m AGL and turn to southwest at higher elevations.

538 Fixed sites A2, A1, and H form a south-north line through the King's Plains wind farm. The
539 lower panels of Figure 14 show wind profiles at these three sites averaged for three time periods
540 from late morning to late afternoon. For the first two time periods, the mean wind speeds at
541 downwind Site H were larger compared to other sites (Figure 14d, e), again contrary to expectation.
542 Radünz et al. (2025) also noticed this effect and attributed the differences to terrain influences that
543 can lead to increased wind speeds downwind.

544

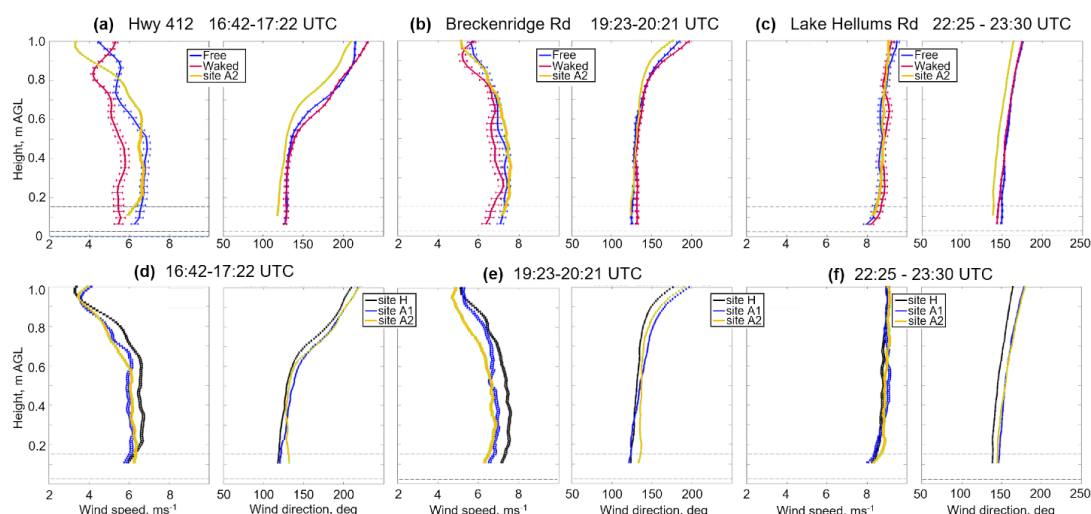
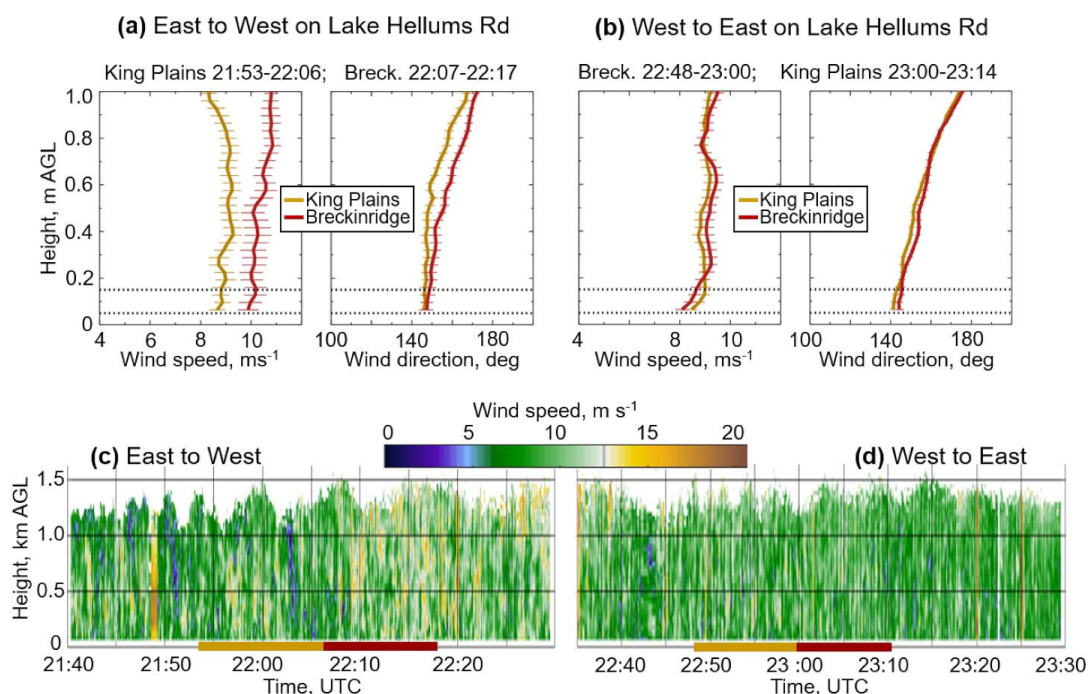


Figure 14. (Top row) Mean profiles of (blue) free and (red) waked wind speed and direction from PUMAS measurements on (a) Hwy 412, (b) Breckenridge Rd., and (c) Phillips Ave. Yellow color indicates inflow wind profiles from stationary Doppler lidar at Site A2 averaged for the corresponding time interval. (Bottom row) Mean wind speed and direction profiles (d–f) from stationary Doppler lidar measurements at sites (black) H, (blue) A1, and (yellow) A2.

The technique allows us to estimate the overall impact of individual wind farms as illustrated in Figure 15. During the ~55 km transect on Lake Hellums Rd., PUMAS passed Breckenridge and King Plains wind farms twice, going east to west and back (Figure 13b, d). The difference in turbine-layer wind flow downstream of both wind farms was about 1.3 m s^{-1} during the EW transect due to a slight increase of wind speeds at 22:07–22:17 UTC (Figure 15c). During the WE transect, winds downstream of both wind farms were almost equal with the mean difference of 0.36 m s^{-1} (Figure 15d). Wind directions in the rotor layer were close for both transects, with differences of 2° .



560

561 Figure 15. Wind speed and direction profiles from PUMAS measurement within the 10 km radius of
 562 influence by turbines from (gold) King Plains and (dark red) Breckinridge wind farms during (a) east to west
 563 and (b) west to east transects along Lake Hellums Rd. (Figure 13). (c, d) Time-height cross sections of wind
 564 speed at these transects. Color bars at the bottom of both panels indicate parts of each transect downstream
 565 of (gold) King Plains and (dark red) Breckenridge wind farms.

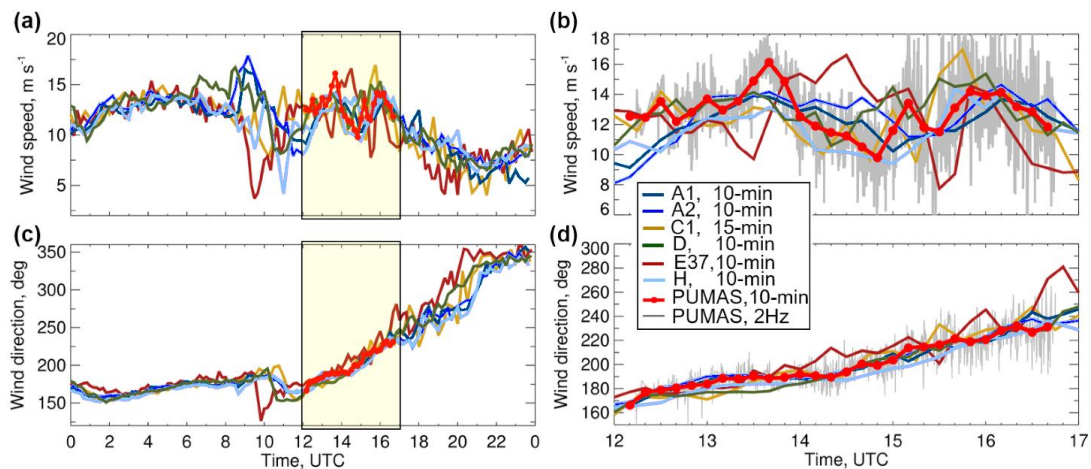
566 The results in Figures 13–15 illustrate the ability to determine free and waked flows on long
 567 (>55 km) transects at various distances (0.9–5 km) from the wind farm and to compare the waked
 568 flow downwind of the Breckinridge and King Plains wind farms. These results are obtained for
 569 moderate ($6\text{--}12\text{ m s}^{-1}$) southeasterly winds and unstable BL conditions of large atmospheric
 570 variability and strong vertical mixing, leading to rapid mixing out of the wakes. Spatial variations
 571 of the free-stream wind speed, often related to small differences in terrain, and temporal changes
 572 were $\sim 1\text{ m s}^{-1}$, which were similar to the differences between waked and free-stream speeds, when
 573 observed. Thus, under these daytime conditions, it was often difficult to distinguish the wakes from
 574 the ambient flow. The following section will show some examples from PUMAS measurements on
 575 5 Sep characterized by stronger ($10\text{--}20\text{ m s}^{-1}$) wind speeds.

576 5.3 5 September case study, nocturnal LLJ, southwesterly winds



Time series of wind speed from PUMAS and six stationary Doppler lidars (Figure 3) taken at the heights closest to the turbine hub height of 90 m are shown in Figure 16 for the diurnal period (Figure 16a) and the period of PUMAS operations (Figure 16b). Wind speed and direction from all lidars show small differences and similar trends from sunset to midnight (0100–0600 UTC). Later in the morning and daytime during PUMAS operations, winds at all sites fluctuate around 10–14 m s⁻¹, later decreasing to 5–8 m s⁻¹ by the evening hours. Wind directions from all lidars show steady turning from southeasterly (~150°) to northerly (~360°). Wind speed and direction for the period of PUMAS measurements at 1200–1700 UTC (yellow box in Figure 16a, b) show similar variations of data from all lidars and close period-mean data (Table 4). Slightly lower (11.6 m s⁻¹) mean wind speed is observed at Site H, located in the wake of turbines for south-southwesterly directions compared to Site D (12.9 m s⁻¹) and Site A2 (12.4 m s⁻¹) of inflow lidar measurements (Table 4). The period-mean wind speed of 2 Hz (Figure 16b, gray) and 10-min averaged (Figure 16b, red) PUMAS measurements are similar (Table 4) but the standard deviation of 2 HZ data is larger (2.3 m s⁻¹) compared to the 0.4 m s⁻¹ standard deviation of 10-min averaged data.

591



592

Figure 16. Wind speed and wind direction at 90–110 m from several AWAKEN stationary Doppler lidars and PUMAS on 5 Se, 2023: (a) Time series of 10 min (15 min at C1) data from stationary lidars at several sites are shown for 24 hours by colors according to the color scale. Data is taken close to the hub height; 90 m at sites C1, E37, D, Pumas, and 110 m at sites A1, A2, H. Yellow boxes indicate the time of PUMAS measurements on this day. (b) Same as (a) but for the period of PUMAS measurements at 1200–1700 UTC. The gray color indicates 2 Hz PUMAS, and the red line with dots shows 10 min averages.



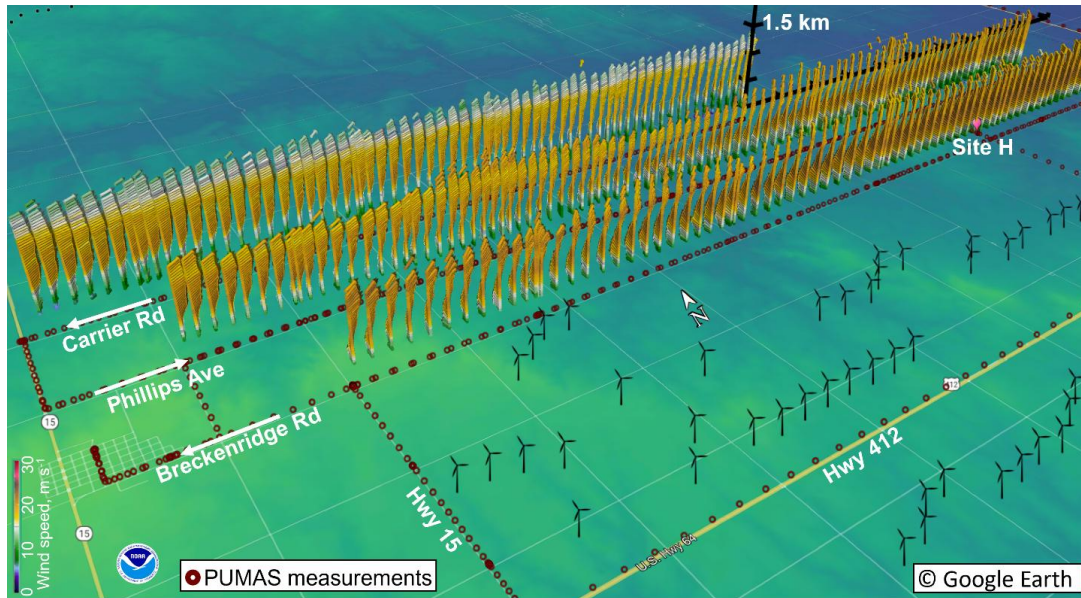
599

600 Table 4. Mean and standard deviation of wind speed and direction from PUMAS and stationary
 601 lidars over period of PUMAS operations on 5 Sep at 1200–1700 UTC.

Site	Height	Time resolution	Speed, m s ⁻¹		Direction, deg	
			<i>mean</i>	<i>STD</i>	<i>mean</i>	<i>STD</i>
PUMAS	90	2Hz	12.8	2.3	201.7	19.7
PUMAS	90	10 min	12.8	1.4	200.2	18.7
C1	90	15 min	12.2	2.0	201.7	26.4
E37	90	10 min	12.3	2.4	209.6	29.3
A1	110	10 min	12.0	1.3	201.3	23.6
A2	110	10 min	12.4	1.8	201.7	21.5
H	110	10 min	11.6	1.4	195.3	22.1
D	90	10 min	12.9	1.2	198.8	24.5

602 An example of wind speed and direction profiles from PUMAS measurements within the
 603 King Plains wind farm is shown in Figure 17 for three (out of 22 total) transects on 5 Sep. Transects
 604 are shown for alternate WE and EW driving directions on Breckenridge Rd., Phillips Ave., and
 605 Carrier Rd. (Figure 17, white arrows). The south-north distance between these roads is 1.6 km. The
 606 length of these transects depends on road conditions and varies from 19.9 km on Breckenridge Rd.
 607 to 12.5 km on Carrier Rd., which ends due to the terrain after crossing County Road 20.

608



609

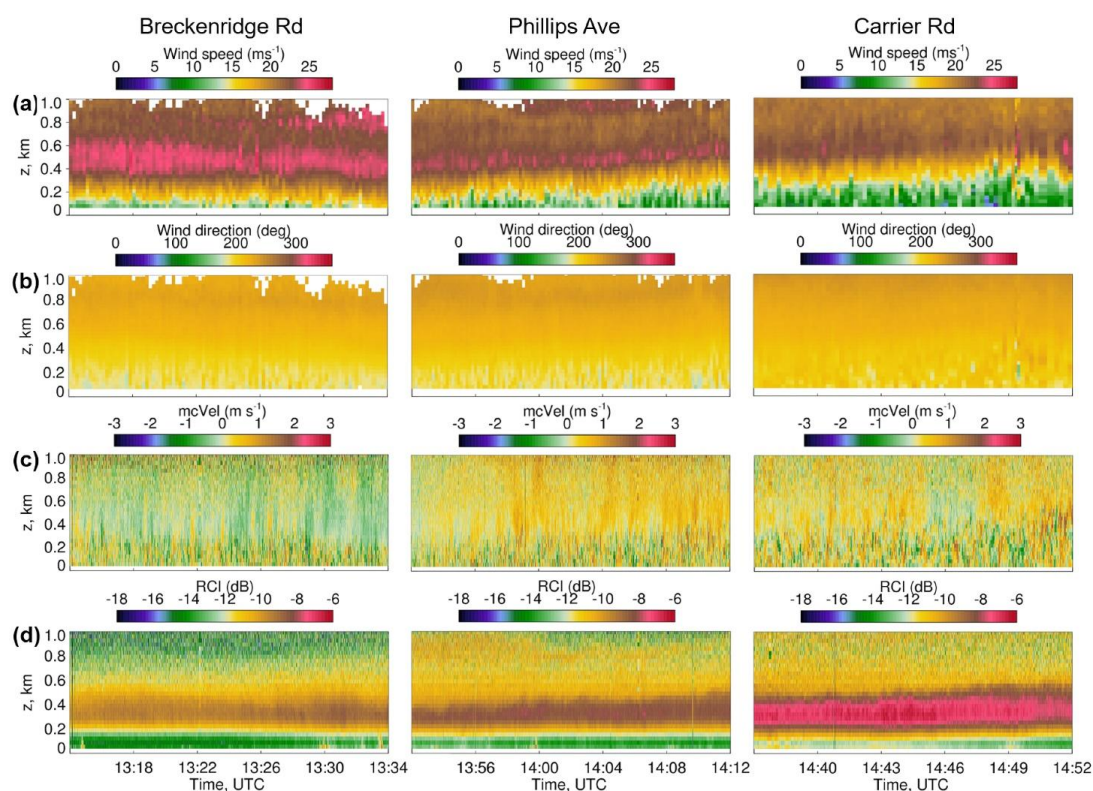
610 Figure 17. Wind speed (colors) and direction (arrows) profiles on 5 Sep are shown along individual transects
 611 on Breckenridge Rd. (1314–1334 UTC), Phillips Ave. (1352–1414 UTC), and Carrier Rd. (1437–1451 UTC)
 612 selected for the analysis. The dark red circles indicate points of PUMAS measurements on 5 Sep. Profiles
 613 are embedded on a Google Earth terrain elevation map (Debnath et al, 2022) and rotated clockwise $\sim 60^\circ$ for
 614 a better view. Wind speed is scaled from 0 to 30 m s^{-1} according to the color scale on the left side of this
 615 figure. The horizontal distance between profiles is about 300 m. White arrows on the left corner indicate the
 616 PUMAS driving direction for each transect in this example.

617 Time-height cross sections (Figure 18) of simultaneously measured wind speed, wind
 618 direction, and motion-corrected vertical velocity along the waked part of the transects from Figure
 619 17 illustrate temporal evolution of wind flows on each transect, as the convective BL mixed upward
 620 into the remaining nighttime LLJ. Wind speeds of $8\text{--}12 \text{ m s}^{-1}$ below 400 m increased to $>25 \text{ m s}^{-1}$
 621 above this height at all transects, with a strong ($>28 \text{ m s}^{-1}$) LLJ within 400–600 m captured during
 622 the 20 min transect at Breckenridge Rd. The LLJ of $\sim 25 \text{ m s}^{-1}$, observed during the 20-min transect
 623 on Phillips Ave, decreased to 20 m s^{-1} at the 15 min transect on Carrier Rd. Wind directions during
 624 all transects are mostly south-southwesterly ($\sim 200^\circ$) with some episodes of southerly winds below
 625 200 m (Figure 18b). The motion-corrected vertical velocity is weaker at Breckenridge Rd. with
 626 more downward motions (Figure 18c), but during all transects more variability is observed in the
 627 growing convective layer at low levels.

628



629



630

631 Figure 18. Time-height cross sections of simultaneously measured (a) wind speed, (b) wind direction, (c)
 632 motion-corrected vertical velocity, and (d) range-corrected backscatter intensity from transects shown in
 633 Figure 17 along (left column) Breckenridge Rd., (middle) Phillips Ave., and (right) Carrier Rd. Panels c, d
 634 are shown up to 2 km AGL to illustrate BL growth.

635

The temporal increase of BL depth can be seen in plots of vertical velocity (Figure 18c) and the range-corrected intensity (Figure 18d). Measurements from stationary lidars have been used extensively to estimate planetary boundary layer mixing height (Bonin et al. 2017), but a similar technique using mobile lidar measurements is currently under development.

639

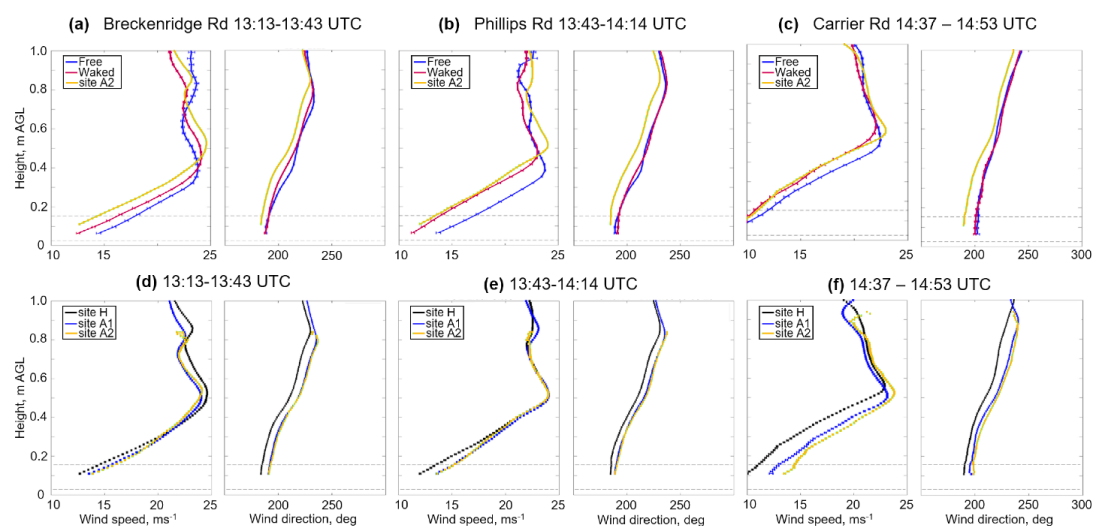
The difference between waked and free flows in the rotor layer during all transects is less than 2 m s^{-1} (Figure 19a–c), and a similar difference for the same time intervals (Figure 19d–f) is found between wind speed measured by stationary lidars at Site A2 (inflow) and Site H (waked). Although the mean wind direction within the rotor layer is south-southwesterly from PUMAS and stationary lidars during all transects, the BL stability changed from stable during the transect on Breckenridge Rd. to unstable during the transect on Carrier Rd. Wind speeds from PUMAS and

644



three stationary lidars decreased with time but for all periods show high shear below LLJ maxima
 at 400–500 m.

647



648

Figure 19. Similar to Figure 14, but for the mean profiles during transects on 5 Sep shown in Figure 17. The embedded plots indicate the BL stability.

6. Conclusions

Quantitative characteristics of wind and turbulence in the atmospheric layers occupied by the wind turbine rotor blades are crucial to wind energy, as is wind information above this layer to provide a meteorological context up to several hundreds of meters AGL. Understanding the variability of winds across wind farms and under different conditions is a key factor in the planning and operations of wind projects.

The high-frequency, motion-compensated PUMAS measurements of the horizontal wind speed, wind direction, range-corrected intensity, and simultaneous vertical-velocity statistics, including variance, skewness, and kurtosis, from a moving platform, provide a new approach to characterizing dynamic processes critical for wind farm wake analysis. The unique PUMAS measurements offer insight into the temporal and vertical variability of wind flows similar to stationary scanning lidars and also reveal spatial variability of characteristics of the horizontal and vertical structure of wind flows modified by operating wind turbines.



664 In the daytime convective cases studied here, spatial variations of the unwaked, free-stream
 665 wind speeds were often $\sim 1 \text{ m s}^{-1}$, and temporal changes along transects repeated over periods of an
 666 hour were of similar magnitude. Differences in waked vs. free-stream speeds, when discernable,
 667 were also $\sim 1 \text{ m s}^{-1}$, so it is often difficult to distinguish turbine or wind-farm wake effects from the
 668 natural atmospheric variability under these conditions.

669 Data from the mobile lidar can also complement the AWAKEN instrumentation to
 670 understand the effect of a large wind farm on wind flows under different background wind
 671 conditions and stratification. The PUMAS measurements can be used to evaluate wind simulation
 672 by models and improve wake model prediction accuracy. The truck-based mobile Doppler lidar
 673 data analyses show that advances in measuring, understanding, and modeling the atmospheric
 674 boundary layer within wind farms will be required to provide improved meteorological support for
 675 wind energy.

676 The developed technique allowed the sampling and automated analysis of wind speeds
 677 influenced by wind turbine clusters located at different distances from PUMAS transects and the
 678 flexibility to adjust the sampling drive patterns to account for any wind directions.

679 **Author contribution:** YP and AB planned the PUMAS measurement campaign, processed and
 680 analyzed the data; BMC, MH, and RM operated the mobile lidar and performed the
 681 measurements; MZ provided remote software support, YP wrote the manuscript draft; RB, ES,
 682 SB, and BC reviewed and edited the manuscript, SL and NB provided data from stationary lidars
 683 and edited the manuscript; PM planned the overall Awaken campaign.

684 **Acknowledgment.** The authors thank the AWAKEN experiment participants who aided in the
 685 deployment and the collection of remote sensing data and our colleagues who monitored, quality
 686 controlled, and provided data to the Data Archive. Funding was provided by the U.S. Department
 687 of Energy Office of Energy Efficiency & Renewable Energy Wind Energy Technologies Office.,
 688 The mobile Doppler lidar measurements in Oklahoma, as part of the AWAKEN field was
 689 supported by the National Oceanic and Atmospheric Administration (NOAA) Atmospheric
 690 Science for Renewable Energy (ASRE) program and by. This research the NOAA cooperative
 691 agreement NA22OAR4320151, for the Cooperative Institute for Earth System Research and Data
 692 Science (CIRESRDS). This work was authored in part by the National Renewable Energy Laboratory
 693 for the U.S. Department of Energy (DOE) under Contract No. DE-AC36-08GO28308. Funding was



provided by the US Department of Energy Office of Energy Efficiency and Renewable Energy Wind Energy Technologies Office. The views expressed in the article do not necessarily represent the views of the CIESRDS, NOAA, DOE or the U.S. Government. The U.S. Government retains and the publisher, by accepting the article for publication, acknowledges that the U.S. Government retains a nonexclusive, paid-up, irrevocable, worldwide license to publish or reproduce the published form of this work, or allow others to do so, for U.S. Government purposes. We thank Amy Brice from NREL for editing the paper according to the journal requirements.

Data availability statement. All the data are publicly available. Datasets from scanning Doppler lidars at the Atmospheric Radiation Measurement (ARM) Southern Great Plains (SGP) sites C1 and E37 are available from the ARM SGP Archive at <https://www.arm.gov/capabilities/observatories/sgp>. Data from scanning Doppler lidars operated during AWAKEN experiment are available from the Atmosphere to Electrons Wind Data Hub (<https://www.a2e.energy.gov>, U.S. Department of Energy, 2024). The lidar data DOI at site A1 is <https://doi.org/10.21947/2375440>, at site A2 is <https://doi.org/10.5439/1890922>, at site H is <https://doi.org/10.21947/2283040>, and at site D is <https://doi.org/10.21947/2375440>. The sonic anemometer data DOI at site A2 is <https://doi.org/10.21947/2375440>. And the NREL ASSIST thermodynamic profiler at site B is <https://doi.org/10.21947/2375440>.

Appendix A. CSL/NOAA Field Projects in 2018–2024 using mobile lidar systems.

Table A1. Mobile Doppler lidar measurements from various platforms.

Platform	Project	Date	Location
Aircraft & Truck	Utah Summer Ozone Study (USOS)	July-Aug 2024	Salt Lake City, Utah
Aircraft	Airborne Methane Mass Balance Emissions in Colorado (AMMBEC)	July 2024	Front Range, Colorado
Aircraft	Airborne and Remote sensing Methane and Air Pollutant Surveys (AiRMAPS)	2024	U.S. East Coast
Truck	Oil and Gas Air Quality Study (DJ-CDPHE II)	Oct-Nov 2023	NW Colorado
Truck	American Wake Experiment (AWAKEN)	Aug-Sep 2023	Central Oklahoma



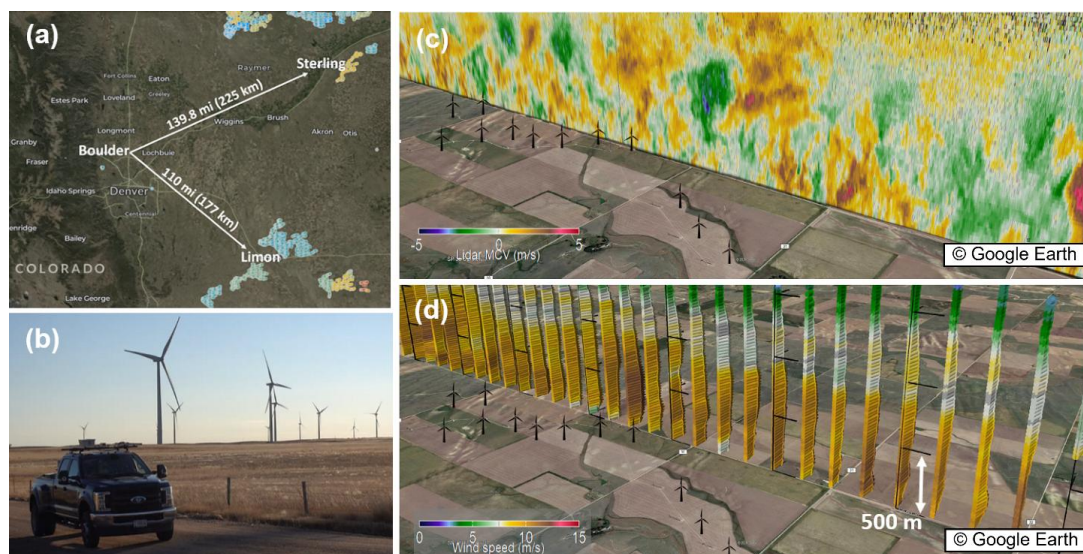
Aircraft	Coastal Urban Plume Dynamics Study (CUPiDS)	June-Aug 2023	New York City Region
Truck	Pilot Studies in Colorado Front Range (PUMAS)	Feb-Mar 2023	Metro Denver, Colorado
Aircraft & Truck	California Fire Dynamics Experiment (CalFiDE)	Aug-Sep 2022	California & Oregon
Aircraft	System Integration and Test Experiment (SITE)	Jun-Aug 2021	Florida
Aircraft & Truck	Southwest Urban NO _x and VOC Experiment (SUNVEx)	Aug 2021	Las Vegas, Nevada, Louisiana, & California
Truck	Oil and Gas Air Quality Study (DJ-CDPHE I)	Sep 2021	Metro Denver, Colorado
Truck	Pilot Studies in Colorado Front Range (PUMAS)	Oct-Nov 2021	Metro Denver, Colorado
Truck	Pilot Studies in Colorado Front Range (PUMAS)	Jun-Oct 2020	Metro Denver, Colorado
Ship	Atlantic Tradewind Ocean-Atm. Interaction Campaign (ATOMIC)	Jan-Feb 2020	Tropical North Atlantic
Aircraft	Fire Influence on Regional to Global Env.& Air Quality (FIREX-AQ)	Jul-Aug 2019	Pacific Northwest
Aircraft	Fire Winds (FIREWinds)	Jun 2018	Florida
Ship	Propagation of Intra-seasonal Tropic Oscillations (PISTON)	Aug-Oct 2018	Philippine Sea



715 Appendix B. Test-drives around wind farms in Colorado

716 Several test-drives of PUMAS were performed around wind farms in Sterling and Limon
 717 located in the northern and southern parts of Colorado (Figure B1 a, b) to obtain information on
 718 system performance, measurement errors, and driving strategies. The data were used to establish
 719 measurement capability to study dynamic processes upwind and downwind of turbines. Figure B1
 720 c shows motion-stabilized vertical velocity obtained from a lidar beam pointing zenith (90°
 721 elevation angle).

722



723

724 Figure B1. (a) A USGS map of wind farms located ~ 200 km to the northeast (near Sterling) or to the
 725 southeast (near Limon) from Boulder, selected for PUMAS test drives in 2020, 2021, and 2023 (Table A1,
 726 Appendix A); (b) a picture of PUMAS driving in the vicinity of wind turbines; (c) Profiles of vertical velocity
 727 along a (~ 22 km) path are shown on Google Earth; (d) Profiles of wind speed (colors) and wind direction
 728 (arrows) along the same path. Black horizontal lines indicate height increments of 500 m.

729 The high temporal (~ 20 s) and vertical (30 m) resolution of these profiles yields unique
 730 information about the extent and strengths of the vertical motions, including thermal updrafts and
 731 turbulence at the cloud base. Measurements from conical scanning at 15° from the zenith (Figure
 732 B1 d) reveal southerly wind speeds of ~ 12 m s $^{-1}$ up to 1.5 km.

733



734 **References:**

- 735 Atmosphere to Electrons (A2e)_1. 2024. awaken/sa2.lidar.z01.c0. Maintained by A2e Data Archive
 736 and Portal for U.S. Department of Energy, Office of Energy Efficiency and Renewable
 737 Energy. DOI: 10.21947/2375440. Accessed: 29 09 2024.
- 738 Atmosphere to Electrons (A2e)_2. 2024. awaken/sa1.lidar.z03.c0. Maintained by A2e Data Archive
 739 and Portal for U.S. Department of Energy, Office of Energy Efficiency and Renewable
 740 Energy. DOI: 10.21947/2375440. Accessed: 29 09 2024.
- 741 Atmosphere to Electrons (A2e)_3. 2024. awaken/sh.lidar.z05.c0. Maintained by A2e Data Archive
 742 and Portal for U.S. Department of Energy, Office of Energy Efficiency and Renewable
 743 Energy. DOI: 10.21947/2375440. Accessed: 29 09 2024.
- 744 Atmosphere to Electrons (A2e)_4. 2024. awaken/sd.lidar.z01.00. Maintained by A2e Data Archive
 745 and Portal for U.S. Department of Energy, Office of Energy Efficiency and Renewable
 746 Energy. DOI: 10.21947/2375440. Accessed: 29 09 2024.
- 747 Atmosphere to Electrons (A2e)_5. 2024. awaken/sa2.sonic.z01.c0. Maintained by A2e Data Archive
 748 and Portal for U.S. Department of Energy, Office of Energy Efficiency and Renewable
 749 Energy. DOI: 10.21947/2375440. Accessed: 29 09 2024.
- 750 Atmosphere to Electrons (A2e)_6. 2024. awaken/sb.assist.z01.c0. Maintained by A2e Data Archive
 751 and Portal for U.S. Department of Energy, Office of Energy Efficiency and Renewable
 752 Energy. DOI: 10.21947/2375440. Accessed: 29 09 2024.
- 753 Aitken, M. L., J. K. Lundquist, R. M. Banta, and Y. L. Pichugina, 2014: Quantifying wind turbine
 754 wake characteristics from scanning remote sensor data. *J. Atmos. Oceanic Technol.*, 31,
 755 765–787, doi:[10.1175/JTECH-D-13-00104.1](https://doi.org/10.1175/JTECH-D-13-00104.1).
- 756 Banta, R. M., R. K. Newsom, J. K. Lundquist, Y. L. Pichugina, R. L. Coulter, and L. Mahrt,
 757 2002: Nocturnal low-level jet characteristics over Kansas during CASES-99. *Bound.-*
 758 *Layer Meteor.*, **105**, 221–252, <https://doi.org/10.1023/A:1019992330866>
- 759 Banta, R.M., Y.L. Pichugina, N. D. Kelley, W. A. Brewer, and R. M. Hardesty, 2013: Wind-energy
 760 meteorology: Insight into wind properties in the turbine rotor layer of the atmosphere from
 761 high-resolution Doppler lidar. *Bull. Amer. Meteor. Soc.*, 94, 883–902, doi:[10.1175/BAMS-](https://doi.org/10.1175/BAMS-D-11-00057.1)
 762 [D-11-00057.1](https://doi.org/10.1175/BAMS-D-11-00057.1).
- 763 Banta, R.M., Y.L. Pichugina, W.A. Brewer, J.K. Lundquist, N.D. Kelley, S.P. Sandberg, R.J.
 764 Alvarez, R.M. Hardesty, and A.M. Weickmann, 2015: 3-D volumetric analysis of wind-



- turbine wake properties in the atmosphere using high-resolution Doppler lidar. *J. Atmos. and Oceanic Tech.*, **32**, 904-914, [Available online at <http://dx.doi.org/10.1175/JTECH-D-14-00078.1>]
- Banta, R. M., Pichugina, Y. L., Brewer, W. A., and Coauthors, 2018: Evaluating and Improving NWP Forecast Models for the Future: How the Needs of Offshore Wind Energy Can Point the Way. *Bull. Amer. Meteor. Soc.*, **99**, 1155–1176, <https://doi.org/10.1175/BAMS-D-16-0310.1>.
- Banta, R.M., Y.L. Pichugina, W.A. Brewer, and Coauthors, 2023, [Measurements and model improvement: Insight into NWP model error using Doppler lidar and other WFI2 measurement systems](#), *Monthly Weather Review*, 152, pp. 3063-3087 doi:10.1175/MWR-D-23-0069.1, 2023.
- Banta, R. M., Y. L. **Pichugina**, and R. K. Newsom, 2003: Relationship between low-level jet properties and turbulence kinetic energy in the nocturnal stable boundary layer. *J. Atmos. Sci.*, **60**, 2549–2555, [https://doi.org/10.1175/1520-0469\(2003\)060%3C2549:RBLJPA%3E2.0.CO;2](https://doi.org/10.1175/1520-0469(2003)060%3C2549:RBLJPA%3E2.0.CO;2)
- Bingöl, F., J. Mann, and G. Larsen, 2010: Light detection and ranging measurements of wake dynamics. Part I: One-dimensional scanning. *Wind Energy*, **13**, 51–61.
- Blackadar, A. K. (1957). Boundary layer wind maxima and their significance for the growth of nocturnal inversions. *Bulletin of the American Meteorological Society*, 38(5), 283-290
- Bodini N., A. Abraham, P. Doubrawa, S. Letizia, R. Thedin, N. Agarwal, B. Carmo, L. Cheung, W. Correa Radunz, A. Gupta, L. Goldberger, N. Hamilton, T. Herges, B. Hirth, G. V. Iungo, A. Jordan, C. Kaul, P. Klein, R. Krishnamurthy, J. K. Lundquist, E. Maric, P. Moriarty, C. Moss, R. Newsom, Y. Pichugina, M. Puccioni, E. Quon, S. Roy, D. Rosencrans, M. Sanchez Gomez, R. Scott, M. Shams Solari, T. J. Taylor, S. Wharton, (2024). An International Benchmark for Wind Plant Wakes from the American WAKE Experiment (AWAKEN): Article No. 092034. *Journal of Physics: Conference Series*, 2767(9). <https://doi.org/10.1088/1742-6596/2767/9/092034>
- Bonin, T. A., B. J. Carroll, R. M. Hardesty, W. A. Brewer, K. Hajny, O. E. Salmon, and P. B. Shepson, 2018: Doppler Lidar Observations of the Mixing Height in Indianapolis Using an Automated Composite Fuzzy Logic Approach. *J. Atmos. Oceanic Technol.*, **35**, 473–490, <https://doi.org/10.1175/JTECH-D-17-0159.1>.



- 796 Brewer, W. A., and R. M. Hardesty, 1995: Development of a dual wavelength CO₂ mini-MOPA
 797 Doppler lidar. Proc. Coherent Laser Radar Conf., Massachusetts, MA, Optical Society of
 798 America, 293–296.
- 799 Browning, K. A. and Wexler, R.: 1968, ‘The Determination of Kinematic Properties of a Wind
 800 Field Using Doppler Radar’, *J. Appl. Meteorol.* **7**, 105–113.
- 801 Debnath, M., Moriarty, P., Krishnamurthy, R., Bodini, N., Newsom, R., Quon, E., Lundquist, J.,
 802 Letizia, S., Iungo, G., and Klein, P. (2023). Characterization of wind speed and directional
 803 shear at the AWAKEN field campaign site. *Journal of Renewable and Sustainable Energy*.
 804 15. 10.1063/5.0139737
- 805 Carroll, B. J., B. B. Demoz, and R. Delgado, 2019: An overview of low-level jet winds and
 806 corresponding mixed layer depths during PECAN. *J. Geophys. Res.*, **124**, 9141–9160,
 807 <https://doi.org/10.1029/2019JD030658>.
- 808 Carroll BJ; Brewer WA; Strobach E; Lareau N; Brown SS; Valero MM; Kochanski A; Clements
 809 CB; Kahn R; Junghenn Noyes KT. (2024). Measuring Coupled Fire–Atmosphere
 810 Dynamics: The California Fire Dynamics Experiment (CalFiDE). *Bulletin of the American*
 811 *Meteorological Society* **105**(3). [10.1175/bams-d-23-0012.1](https://doi.org/10.1175/bams-d-23-0012.1).
- 812 Debnath, M., Scholbrock, A., Zalkind, D., Moriarty, P., Simley, E., Hamilton, N., Ivanov, C.,
 813 Arthur, R., Barthelmie, R., Bodini, N., Brewer, A., Goldberger, L., Herges, T., Hirth, B.,
 814 Iungo, G., Jager, D., Kaul, C., Klein, P., Krishnamurthy, R., ... Wharton, S. (2022). Design
 815 of the American Wake Experiment (AWAKEN) Field Campaign. *Journal of Physics:*
 816 *Conference Series*, **2265**(2), Article No. 022058. [https://doi.org/10.1088/1742-](https://doi.org/10.1088/1742-6596/2265/2/022058)
 817 [6596/2265/2/022058](https://doi.org/10.1088/1742-6596/2265/2/022058), <https://doi.org/10.1088/1742-6596/2265/2/022058>
- 818 Djalalova, I. V., J. Olson, J. R. Carley, L. Bianco, J. M. Wilczak, Y. Pichugina, R. Banta, M.
 819 Marquis, J. Cline, 2016: The POWER experiment: Impact of assimilation of a network of
 820 coastal wind profiling radars on simulating offshore winds in and above the wind turbine
 821 layer. *Weather and Forecasting*, **31**, 1071–1091, doi: [http://dx.doi.org/10.1175/WAF-D-15-](http://dx.doi.org/10.1175/WAF-D-15-0104.1)
 822 [0104.1](http://dx.doi.org/10.1175/WAF-D-15-0104.1)
- 823 Geerts, B., Parsons, D., Zieglgler, C. L., Weckwerth, T. M., Bigggerstaff, M. I., Clark, R. D., et
 824 al. (2017). The 2015 plains elevated convection at night field project. *Bulletin of the*
 825 *American Meteorological Society*, **98**(4), 767–786. [https://doi.org/10.1175/BAMS-D-15-](https://doi.org/10.1175/BAMS-D-15-00257.1)
 826 [00257.1](https://doi.org/10.1175/BAMS-D-15-00257.1)



- 827 Grund, C. J., Banta, R.M., George, J. L., Howell, J. N., Post, M. J., Richter, R. A., and
 828 Weickmann, A.M., 2001: High-Resolution Doppler Lidar for Boundary-Layer and Cloud
 829 Research, *J. Atmos. Ocean. Tech.* **18**, 376–393.
- 830 Krishnamurthy R., R.K. Newsom, D. Chand, and W.J. Shaw. 2021. *Boundary Layer Climatology*
 831 *at ARM Southern Great Plains*. PNNL-30832. Richland, WA: Pacific Northwest National
 832 Laboratory. (2021), 10.2172/1778833.
- 833 Krishnamurthy, R., Newsom, R., Kaul, C., Letizia, S., Pekhour, M., Hamilton, N., Chand, D.,
 834 Flynn, D., Bodini, N., & Moriarty, P. (2025). Observations of Wind Farm Wake Recovery
 835 at an Operating Wind Farm. *Wind Energy Science*, 10(2), 361-380.
 836 <https://doi.org/10.5194/wes-10-361-2025>
- 837 Letizia, Stefano, Nicola Bodini, Peter Brugger, Andrew Scholbrock, Nicholas Hamilton,
 838 Fernando Porté-Agel, Paula Doubrawa, and Patrick Moriarty, 2023: Holistic scan
 839 optimization of nacelle-mounted lidars for inflow and wake characterization at the RAAW
 840 and AWAKEN field campaigns. *Journal of Physics: Conference Series*, vol. 2505, no. 1,
 841 p. 012048. IOP Publishing, 2023
- 842 Meneveau, C. (2012). The top-down model of wind farm boundary layers and its applications.
 843 *Journal of Turbulence*, 13. <https://doi.org/10.1080/14685248.2012.663092>
- 844 Michaud-Belleau, V., Gaudreau, M., Lacoursière, J., Boisvert, É., Ravelomanantsoa, L., Turner,
 845 D. D., and Rochette, L., 2025: The Atmospheric Sounder Spectrometer by Infrared
 846 Spectral Technology (ASSIST): Instrument design and signal processing, EGU sphere
 847 [preprint], <https://doi.org/10.5194/egusphere-2024-3617>, 2025. Moriarty, P., Bodini, N.,
 848 Letizia, S., Abraham, A., Ashley, T., Barfuss, K., Barthelmie, R., Brewer, A., Brugger, P.,
 849 Feuerle, T., Frere, A., Goldberger, L., Gottschall, J., Hamilton, N., Herges, T., Hirth, B.,
 850 Hung, L.-Y., Iungo, G. V., Ivanov, H. & Kaul, C. & 18 others. (2024). Overview of
 851 Preparation for the American WAKE Experiment (AWAKEN). *Journal of Renewable*
 852 *and Sustainable Energy*, 16(5). <https://doi.org/10.1063/5.0141683>
- 853 Newsom, R.K. and Krishnamurthy R, 2020: Doppler Lidar (DL) Instrument Handbook, DOE/SC-
 854 ARM-TR-101
- 855 Olson, J. B., and Coauthors, 2019: Improving Wind Energy Forecasting through Numerical
 856 Weather Prediction Model Development. *Bull. Amer. Meteor. Soc.*, **100**, 2201–2220,
 857 <https://doi.org/10.1175/BAMS-D-18-0040.1>.



- 858 Pichugina, Y. L., and R. M. Banta, 2010: Stable boundary-layer depth from high-resolution
 859 measurements of the mean wind profile. *J. Appl. Meteor. Climatol.*, **49**, 20–35, doi:
 860 <https://doi.org/10.1175/2009JAMC2168.1> Pichugina, Y. L., Banta, R. M., Brewer, W. A.,
 861 Kenyon, J., Olson, J. B., Turner, D. D., Wilczak, J., Baidar, S., Lundquist, J. K., Shaw, W.
 862 J., & Wharton, S. (2022). Model Evaluation by Measurements from Collocated Remote
 863 Sensors in Complex Terrain, *Weather and Forecasting*, **37**(10), 1829–1853.
 864 <https://doi.org/10.1175/WAF-D-21-0214.1>
- 865 Pichugina, Y. L., R. M. Banta W. A. Brewer, S. P. Sandberg, and R. M. Hardesty, 2012: Doppler
 866 lidar–based wind-profile measurement system for offshore wind-energy and other marine
 867 boundary layer applications. *J. Appl. Meteor. Climatol.*, **51**, 327–349, doi:[10.1175/JAMC-](https://doi.org/10.1175/JAMC-D-11-040.1)
 868 [D-11-040.1](https://doi.org/10.1175/JAMC-D-11-040.1)
- 869 Pichugina, Y. L., R. M. Banta, W. A. Brewer, D. D. Turner, V. O. Wulfmeyer, E. J. Strobach, S.
 870 Baidar, and B. J. Carroll, 2023: Doppler Lidar Measurements of Wind Variability and LLJ
 871 Properties in Central Oklahoma during the August 2017 Land–Atmosphere Feedback
 872 Experiment. *J. Appl. Meteor. Climatol.*, **62**, 947–969, [https://doi.org/10.1175/JAMC-D-22-](https://doi.org/10.1175/JAMC-D-22-0128.1)
 873 [0128.1](https://doi.org/10.1175/JAMC-D-22-0128.1).
- 874 Pichugina, Y. L., Banta, R. M., Olson J. B., A., Carley J. R., Marquis, M. C., Brewer, W. A., and
 875 Coauthors, 2017a: Assessment of NWP Forecast Models in Simulating Offshore Winds
 876 through the Lower Boundary Layer by Measurements from a Ship-Based Scanning Doppler
 877 Lidar. *Mon. Wea. Rev.*, **145**, 4277–4301, <https://doi.org/10.1175/MWR-D-16-0442.1>.
- 878 Pichugina, Y.L., R.M. Banta, E.J. Strobach, B.J. Carroll, W.A. Brewer, D.D. Turner, V.
 879 Wulfmeyer, E. James, T.R. Lee, S. Baidar, J.B. Olson, R.K. Newsom, H.-S. Bauer, and R.
 880 Rai, 2024: Case study of a bore wind-ramp event from lidar measurements and HRRR
 881 simulations over ARM Southern Great Plains, *Journal of Renewable and Sustainable*
 882 *Energy*, <https://doi.org/10.1063/5.0161905>.
- 883 Pichugina, Y. L., W.A. Brewer, R.M. Banta, L. Bianco, C. Draxl, J. Kenyon, J. K. Lundquist, J.B.
 884 Olson, D.D. Turner, S. Wharton J. Wilczak, S. Baidar, L.K. Berg, H.J.S. Fernando, B.J.
 885 McCarty, R. Rai, B. Roberts, J. Sharp, W.J. Shaw, M.T. Stoelinga, and R. Worsnop, 2020.
 886 Evaluating the WFIP2 updates to the HRRR model using scanning Doppler lidar
 887 measurements in the complex terrain of the Columbia River Basin, *J. Renewable and*
 888 *Sustainable Energy (JRSE)*, **12**(4):27 pp. (2020). <https://doi.org/10.1063/5.0009138>



- 889 Pichugina, Y. L., Brewer, W. A., Banta, R. M., Choukulkar, A., Clack, C. T. M., Marquis, M. C.,
 890 McCarty, B. J., Weickmann, A. M., Sandberg, S. P., Marchbanks, R. D., and Hardesty, R.
 891 M. (2017b) Properties of the offshore low-level jet and rotor layer wind shear as measured
 892 by scanning Doppler lidar. *Wind Energy*, 20:987–1002, doi:
 893 <https://doi.org/10.1002/we.2075>.
- 894 Post MJ, Cupp RE. Optimizing a pulsed Doppler lidar. *Appl Opt*. 1990;**29**(28):4145-58.
 895 [https://doi: 10.1364/AO.29.004145](https://doi.org/10.1364/AO.29.004145). PMID: 20577357.
- 896 Radünz, W., Carmo, B., Lundquist, J. K., Letizia, S., Abraham, A., Wise, A. S., Sanchez Gomez,
 897 M., Hamilton, N., Rai, R. K., and Peixoto, P. S.: Influence of simple terrain on the spatial
 898 variability of a low-level jet and wind farm performance in the AWAKEN field campaign,
 899 Wind Energ. Sci. Discuss. [preprint], <https://doi.org/10.5194/wes-2024-166>, in review,
 900 2025.
- 901 Schroeder, P., W.A. Brewer, A. Choukulkar, A. Weickmann, M. Zucker, M. Holloway, and S.
 902 Sandberg, A compact, flexible, and robust micro pulsed Doppler Lidar, Journal of
 903 Atmospheric and Oceanic Technology, doi:10.1175/JTECH-D-19-0142.1, 2020.
- 904 Smalikho, I.N., V.A. Banakh, Y.L. Pichugina, W.A. Brewer, R.M. Banta, J.K. Lundquist, and N.D.
 905 Kelley, 2013: Lidar Investigation of Atmosphere Effect on a Wind Turbine Wake. *J. Atmos.*
 906 *Oceanic Technol.*, **30**, 2554–2570, <https://doi.org/10.1175/JTECH-D-12-00108.1>
- 907 Strobach EJ; Carroll BJ; Baidar S; Brown SS; Ahmadov R; Brewer WA; Pichugina Y; Makowiecki
 908 A; Peischl J; Zuraski K. (May 28, 2024). A Case Study Featuring the Time Evolution of a
 909 Fire-Induced Plume Jet Over the Rum Creek Fire: Mechanisms, Processes, and Dynamical
 910 Interplay. *Journal of Geophysical Research: Atmospheres* (May 14 2024)**129**(10).
 911 [10.1029/2023jd040483](https://doi.org/10.1029/2023jd040483).
- 912 Strobach, E. J., Brewer, W.A., Senff, C. J., Baidar, S., and McCarty, B., 2023: Isolating and
 913 Investigating Updrafts Induced by Wildland Fires Using an Airborne Doppler Lidar
 914 During FIREX-AQ. *Journal of Geophysical Research: Atmospheres*, **128**(14),
 915 e2023JD038809. <https://doi.org/10.1029/2023JD038809>
- 916 Squitieri, B. J., and W. A. Gallus , 2016: WRF Forecasts of Great Plains Nocturnal Low-Level Jet-
 917 Driven MCSs. Part II: Differences between Strongly and Weakly Forced Low-Level Jet
 918 Environments. *Wea. Forecasting*, **31**, 1491–1510, [https://doi.org/10.1175/WAF-D-15-](https://doi.org/10.1175/WAF-D-15-0150.1)
 919 [0150.1](https://doi.org/10.1175/WAF-D-15-0150.1)



- 920 Sun J, L. Mahrt, R. M. Banta and Y. L. Pichugina, 2012; Turbulence Regimes and Turbulence
 921 Intermittency in the Stable Boundary Layer during CASES-99, *Journal of the Atmospheric*
 922 *Sciences*, Jan. 2012, Vol. **69**, No. 1, pp 338-351
- 923 Turner, D.D., and W.G. Blumberg, 2019: Improvements to the AERIoe thermodynamic profile
 924 retrieval algorithm. *IEEE J. Selected Topics Appl. Earth Obs. Remote Sens.*, 12, 1339-1354,
 925 doi:10.1109/JSTARS.2018.2874968.
- 926 Turner, D.D., and U. Loehnert, 2014: Information content and uncertainties in thermodynamic
 927 profiles and liquid cloud properties retrieved from the ground-based Atmospheric Emitted
 928 Radiance Interferometer (AERI). *J. Appl. Meteor. Clim.*, 53, 752-771, doi:10.1175/JAMC-
 929 D-13-0126.1
- 930 Wilczak, J., and Coauthors, 2019b: The Second Wind Forecast Improvement Project (WFIP2):
 931 Observational field campaign. *Bull. Amer. Meteor. Soc.*, **100**, 1701–1723,
 932 <https://doi.org/10.1175/BAMS-D-18-0035.1>.
- 933 Wulfmeyer, V., D.D. Turner, B. Baker, R. Banta, A. Behrendt, T. Bonin, W.A. Brewer, M. Buban,
 934 A. Choukulkar, E. Dumas, RM Hardesty, T Heus, J Ingwersen, D Lange, TR Lee, S
 935 Metzendorf, SK Muppa, T. Meyers, R Newsom, M Osman, S Raasch, J Santanello, C Senff,
 936 F Späth, T Wagner, T Weckwerth, 2018: “A new research approach for observing and
 937 characterizing land-atmosphere feedback.” *Bull. Amer. Meteor. Soc.*, **99**(8), 1639-1667,
 938 <http://dx.doi.org/10.1175/BAMS-D-17-0009.1>.